Pedro Daniel Marques Mesquita

Robot Control in the Presence of Cardiac Motion

March 2018

· U C ·

Universidade de Coimbra

FCTUC FACULDADE DE CIÊNCIAS
E TECNOLOGIA
UNIVERSIDADE DE COIMBRA

Robot Control in the Presence of Cardiac Motion

Pedro Daniel Marques Mesquita

Coimbra, March 2018

Robot Control in the Presence of Cardiac Motion

Supervisor:

Prof. Doctor Rui Pedro Duarte Cortesão

Co-Supervisor:

Doctor Luís Carlos Vitória dos Santos

Jury:

Prof. Doctor Rui Paulo Pinto da Rocha

Prof. Doctor Rui Pedro Duarte Cortesão

Prof. Doctor Tony Richard de Oliveira de Almeida

Dissertation submitted to the Electrical and Computer Engineering Department of the Faculty of Sciences and Technology of the University of Coimbra in partial fulfilment of the requirements for the Degree of Master of Science.

Coimbra, March 2018

Agradecimentos

Ao Professor Doutor Rui Pedro Duarte Cortesão por todo o conhecimento e ensinamentos transmitidos, pelo tempo dedicado, conselhos e comentários que se tornaram indispensáveis à composição destas páginas.

Ao Doutor Luís Carlos Vitória dos Santos, que sempre demonstrou apoio e se disponibilizou para ajudar mesmo quando se encontrava na fase final da sua dissertação.

À minha família, e em especial aos meus pais, pelo apoio incondicional e enorme paciência ao longo deste percurso. À minha irmã por dizer as coisas tais como elas são. Ao meu irmão por nunca me julgar e à sua enorme compreensão.

À Filipa, por todos os dias que passou ao meu lado, para me ajudar e motivar.

Aos meus amigos, com os quais posso sempre contar.

Um agradecimento especial e com carinho à minha avó Augusta, que certamente teria orgulho desta minha façanha.

Resumo

As doenças cardiovasculares são a causa número um de mortes no mundo, sendo que, entre estas, a doença coronária tem uma das maiores taxas de mortalidade. Posto isto, de forma a reduzir o potencial risco de morte associado a este tipo de patologia, a revascularização miocárdica é um dos procedimentos mais comummente utilizados. Não obstante e, embora se trate de um procedimento devidamente estudado, desenvolvido e, portanto, já maduro, ainda existe um conjunto de riscos que lhe estão associados. Esta cirurgia requer uma esternotomia mediana e um bypass cardiopulmonar (CPB) para manter a circulação e oxigenação sanguíneas, enquanto o coração está parado. Todavia, a cirurgia de peito aberto com recurso a uma máquina de coração-pulmão, conduz regularmente a traumatismos e infecções significativas podendo mesmo, em última instância, provocar a morte.

O conjunto de efeitos secundários e perigos associados a esse tipo de procedimento tem suscitado a pesquisa de alternativas. Neste sentido, a revascularização miocárdica minimamente invasiva e o uso de estabilizadores mecânicos são duas possibilidades. Ora, os estabilizadores mecânicos, enquanto possíveis substitutos do CPB, são colocados em torno da área de interesse de forma a mitigar os movimentos cardíacos. No entanto, o movimento residual continua a ser de tal forma significativo que as lesões no tecido cardíaco continuam a ser um efeito colateral recorrente. Neste sentido, a cirurgia roboticamente assistida, a qual ganhou grande visibilidade e popularidade com o aparecimento dos sistemas cirúrgicos *Zeus* e *da Vinci*, tem o potencial para solucionar este tipo de problemas.

Ao longo da presente dissertação, uma arquitectura de controlo de feedback de força, baseada em observadores activos (filtros de Kalman modificados), é usada e testada de modo a compensar movimentos fisiológicos com seguimento de uma força de referência. Numa fase posterior, as capacidades de telemanipulação da arquitectura de controlo proposta são testadas enquanto proporcionam um feedback háptico. Este é um grande passo no sentido

de desenvolver uma aplicação para o utilizador final, viável para um uso real em cirurgia.

Palavras-Chave

Observador Activo; Filtro de Kalman; Telemanipulação; Cirurgia em Coração a Bater

Abstract

Cardiovascular diseases are the number one cause of death in the world and, among these, coronary heart diseases have the highest mortality rate. In order to reduce the risk of death, coronary artery bypass grafting (CABG) is one of the most common procedures but, despite the fact that it is a studied, developed and well mature procedure, many risks are still involved. The surgery requires a median sternotomy and a cardiopulmonary bypass (CPB) to maintain blood circulation and oxygenation while the heart is stopped. However, open-chest surgery with the use of a heart-lung machine regularly leads to significant trauma and infection and may even lead to death.

The side-effects associated to this type of procedure have motivated the search for alternatives, such as minimally invasive CABG (MICABG) and the use of mechanical stabilizers. Mechanical stabilizers are a substitute to CPB and by placing them around the area of interest they attempt to mitigate heart motion. However, great residual motion remains and injuries to the heart tissue are another side-effect. Robotic assisted surgery has the potential to solve these issues. With the appearance of the *Zeus* and the *da Vinci* surgical systems, robotic assisted surgery gained popularity and viability.

In this thesis, a force feedback control architecture, based in active observers (modified Kalman filters), is used and tested to compensate physiological motion while tracking a reference force. Then, the telemanipulation capabilities of the proposed control architecture are tested, while also providing haptic feedback. This is a major step towards developing an end-user application, viable for use in actual surgery.

Keywords

Active Observer; Kalman filter; Telemanipulation; Beating Heart Surgery

"There should be no boundaries to human endeavour."

— Stephen Hawking, *A Brief History of Time*

Contents

List of Acronyms

AOB	Active Observer
ARMC	Active Relative Motion Cancelling
CABG	Coronary Artery Bypass Grafting
CAD	Coronary Artery Disease
CHD	Coronary Heart Disease
CPB	Cardiopulmonary Bypass
CVD	Cardiovascular Disease
DoF	Degrees-of-Freedom
ECG	Electrocardiogram
GPC	Generalized Predictive Controller
ILC	Iterative Learning Control
LAD	Left Anterior Descending Coronary Artery
MCI	Motion Compensation Instrument
MICABG	Minimally Invasive Coronary Artery Bypass Grafting
PCI	Percutaneous Coronary Interventions
PSD	Power Spectral Density
PSM	Patient Side Manipulator
RMS	Root Mean Square

RMSE	Root Mean Square Error
WAM	Whole Arm Manipulator

List of Symbols

η_k	Uncertainty associated with the measures, see equation (2.16), page 14
$\hat{\Lambda}$	Λ estimation, see equation (2.9), page 12
$\hat{F}_e$	Interaction force estimation, see equation (2.9), page 12
$\hat{g}_x$	g_x estimation, see equation (2.9), page 12
$\hat{K}_s$	Estimativa de K_s, see equation (2.52), page 21
$\hat{V}_x$	V_x estimation, see equation (2.9), page 12
Λ	Cartesian space mass matrix, see equation (2.2), page 11
τ	Generalized joint torque, see equation (2.1), page 11
τ_c	Command torque, page 11
τ_e	Interaction torque, page 11
τ_f	Friction torque, page 11
$\upsilon(q, \dot{q})$	Vector of Coriolis and centripetal forces, see equation (2.1), page 11
$\xi_{x_{r,k}}$	Uncertainty associated with the system, see equation (2.16), page 14
$f^\star$	Control input parameter, see equation (2.9), page 12
F_c	Cartesian force at the end-effector, see equation (2.2), page 11
F_e	Interaction force, see equation (2.2), page 11
$g(q)$	Gravity term, see equation (2.1), page 11
g_x	Cartesian space gravity term, see equation (2.2), page 11

J	Jacobian matrix, see equation (2.3), page 11
K_2	Damping gain, see equation (2.11), page 12
K_k	Kalman gain, see equation (2.34), page 16
K_s	Environment stiffness, see equation (2.11), page 12
$M(q)$	Robot mass matrix, see equation (2.1), page 11
p_k	Active state, see equation (2.20), page 14
Q_k	System noise matrix, see equation (2.35), page 17
R_k	Measurement noise matrix, see equation (2.34), page 16
T_d	Time delay, see equation (2.11), page 12
V_x	Cartesian space vector of Coriolis and centripetal forces, see equation (2.2), page 11
X	Cartesian position, see equation (2.2), page 11

List of Figures

List of Tables

1 Introduction

1.1 Motivation

Cardiovascular diseases (CVD) are the number one cause of death in the world, with an estimated 17.7 million deaths in 2015 alone, amounting to 31% of all global deaths. Avoiding risk behaviours[1], coupled with medication in necessary cases such as patients with diabetes, is the best way to mitigate CVDs and can prevent nearly 75% of all recurring vascular events. Nevertheless, in some cases surgery is needed [World Health Organization, 2017].

Among the CVDs, coronary heart diseases (CHD) have the highest mortality rates, with an approximate total of 7.4 million deaths in 2015. The most common procedures to address CHDs are Percutaneous Coronary Interventions (PCI) and Coronary Artery Bypass Grafting (CABG) with approximately 4,027.3 and 702.5 thousand procedures in 2016, respectively [MedMarket Diligence, 2016]. Both procedures are mature and capable of producing good results, nonetheless CABG appears to offer better results for patients with multi-vessel coronary artery diseases (CAD) [Investigators, 2002] [Serruys et al., 2009].

PCI is a simple intervention to treat narrowing (stenosis) of the coronary arteries. During the procedure, a balloon catheter (with or without a stent) is inserted through the femoral or radial artery and guided to the obstructed artery. Once there, the balloon is inflated to force the vessel to attain the desired width. The use of a stent ensures that the artery remains open (Figure 1.1).

On the other hand, CABG consists in the use of grafts, composed of veins or arteries from other parts of the patients body in order to reroute the blood around a clogged artery, thus normalising blood flow. To this effect it is normally required a sternotomy [2] so the surgeon may access the heart, and a cardiopulmonary bypass (CPB) through the use of a

[1] For instance, lack of exercise, smoking, obesity and alcohol abuse.

[2] A 16 - 20 [cm] incision along the thorax.

heart-lung machine (or extra-corporeal circulation machine) to maintain blood circulation and oxygenation while the heart is stopped [American Heart Association, 2017]. Open-chest surgery, albeit the ease of access and visibility it confers, comes with possible strong repercussions to the patient. Significant trauma and infection are regular side-effects to this procedure [Klesius et al., 2004]. CPB is the major source of complications and it may lead to negative effects on the patient including, but not limited to, postperfusion syndrome and overall infection [Slogoff et al., 1982] [Ascione et al., 2000], therefore motivating the search for new solutions that do not require it.

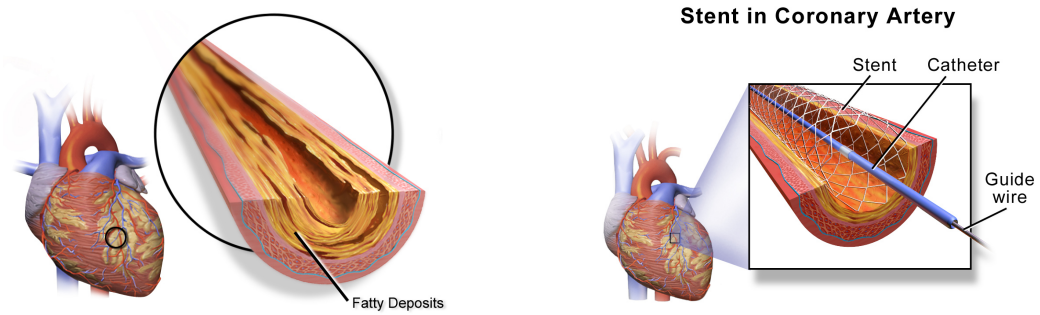

(a) A clogged artery before the PCI procedure.

(b) Methodology used to perform a PCI with a stent.

Figure 1.1: The PCI procedure (source: [Larsson, 2015]).

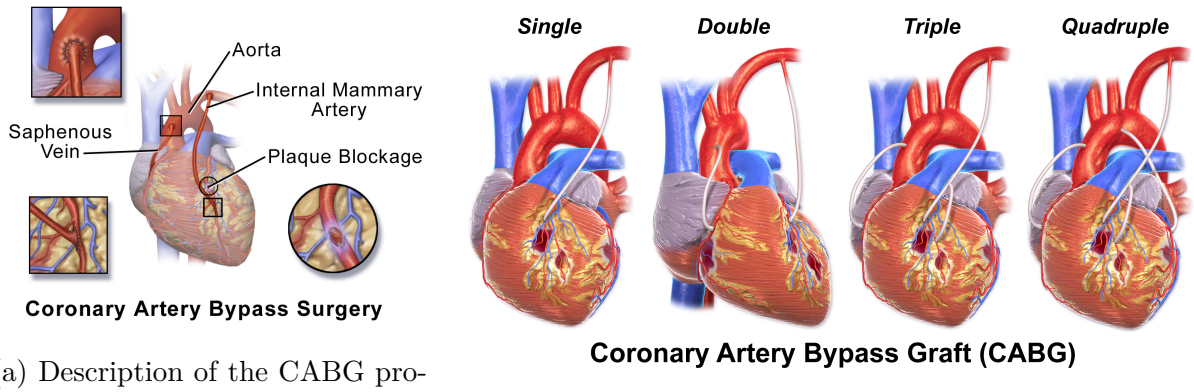

(a) Description of the CABG procedure.

(b) Different types of CABG.

Figure 1.2: The CABG procedure (source: [Larsson, 2015]).

1.2 State of the Art

The practice of CABG with sternotomy and the assistance of CPB has come into use in the late 1960s, with close to sixty years of practice it has matured into an intervention with high success rates, nonetheless the negative effects of CPB and the sternotomy are not negligible. In [Lönn et al., 1999] the use of an axial blood flow pump has been implemented as a possible substitute for CPB, with the intent of allowing a less-invasive approach to CABG and to mitigate some of the complications adjacent to CPB. The axial blood flow pump used was the Hemopump, which was inserted into the left ventricle through a graft sutured to the aorta, 5 to 6 cm distal to the aortic valve, drawing blood from the left ventricle and ejecting it into the descending aorta, thus ensuring a continuous blood flow. This is coupled with the administration of a drug to lower heart rate until the surgeon feels that the heart is flaccid enough to preform surgery. This approach showed good results and proved to be a viable substitute to CPB in terms of the end-result, without many of the possible repercussions that come with the use of CPB. It is however no longer in use.

The need for on-pump cardiac surgery arises from the necessity to mitigate cardiac motion, as such the use of mechanical stabilizers is a good alternative allowing for off-pump cardiac surgery. Mechanical stabilizers fall within two categories: (1) mechanical pressure stabilizers and (2) suction stabilizers. Both are shaped like two-pronged forks and are placed with the prongs on either side of the target artery (Figure 1.3) and by either applying downward pressure (mechanical pressure stabilizer) or by applying vacuum pressure (suction stabilizer) the heart motion is mitigated [Hart et al., 2002]. Studies show that mechanical stabilizers, despite reducing cardiac motion, still allow for significant displacement of the coronary artery ranging from 1.5 to 2.4 mm [Lemma et al., 2005]. Mechanical stabilizers are, therefore, not an optimal solution considering that the residual motion must be manually compensated by the surgeon, the pressure exerted on the heart may cause severe heart damage and the problems associated with the sternotomy remain.

Minimally invasive coronary artery bypass grafting (MICABG) is an approach that seeks to abolish the need for both the CPB and the sternotomy. It has come into fruition through a series of attempts in performing CABG without the need for CPB, that began as early as 1967 when Kolessov reported a bypass to the left anterior descending coronary artery (LAD) and marginal branch of the circumflex coronary artery without CPB through a left

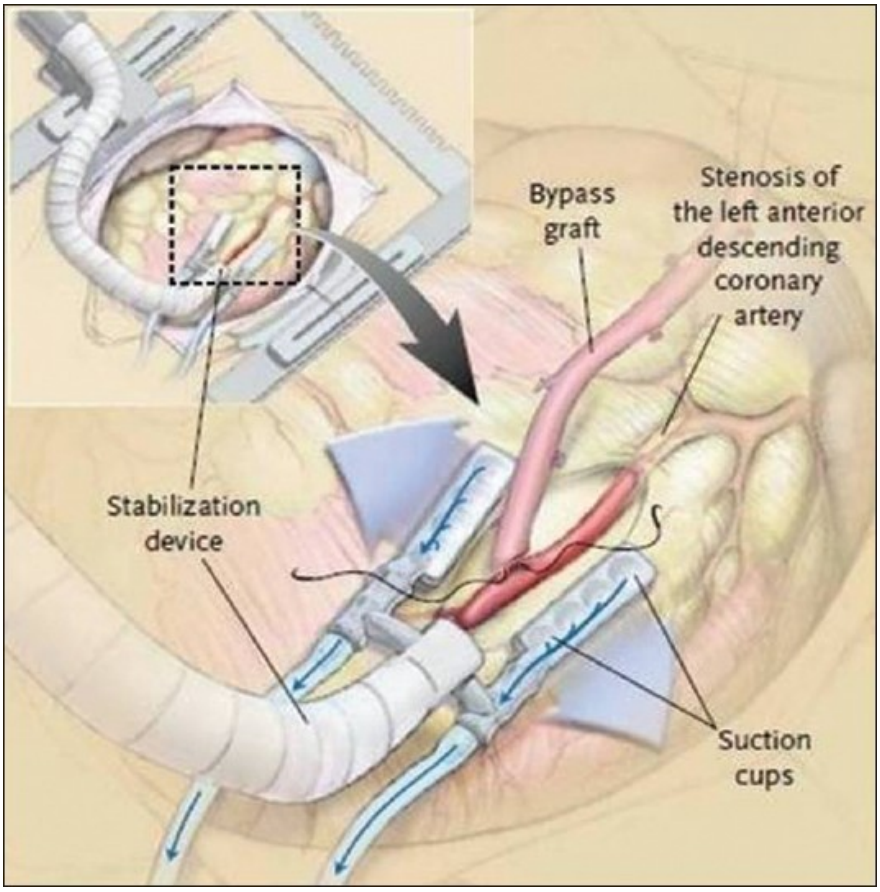

Figure 1.3: Suction Stabilizer (source: [Hemmerling et al., 2013]).

thoracotomy [Kolessov, 1967]. In 1994, Benetti and co-authors suggested that CABG could be performed through a small left thoracotomy with the aid of a thoracoscope [Benetti FJ, Ballester C, 1994]. However this approach still relies on drugs and/or mechanical stabilizers in order to minimize heart motion and, ultimately, the surgeon must compensate residual motion manually. In the late 1990s, with the appearance of the *Da Vinci* and *ZEUS* surgical robot systems, this approach gained renewed support with the first robotic assisted MICABG performed with recourse to the ZEUS surgical robotic system in 1999.

In [Trejos et al., 1999] a heart-tracking hand support is designed to allow beating heart surgery. This device consists of a three-degree-of-freedom motion platform to which the surgeons hand is attached and, with resource to distance information, maintains a constant distance between the support and the heart (Figure 1.4). There is also a camera attached to the motion platform so as to provide a stable view of the surgical site. The obtained results show that performing a task with the hand attached to the moving platform leads to lower execution times and an improved accuracy when compared to the execution of the same task without the hand attached. This solution also eliminates the need for a costly master-slave

station or the use of conventional methods (e.g. mechanical stabilizers). However, it is assumed that near-zero relative motion between the moving platform and the surgical site can be achieved.

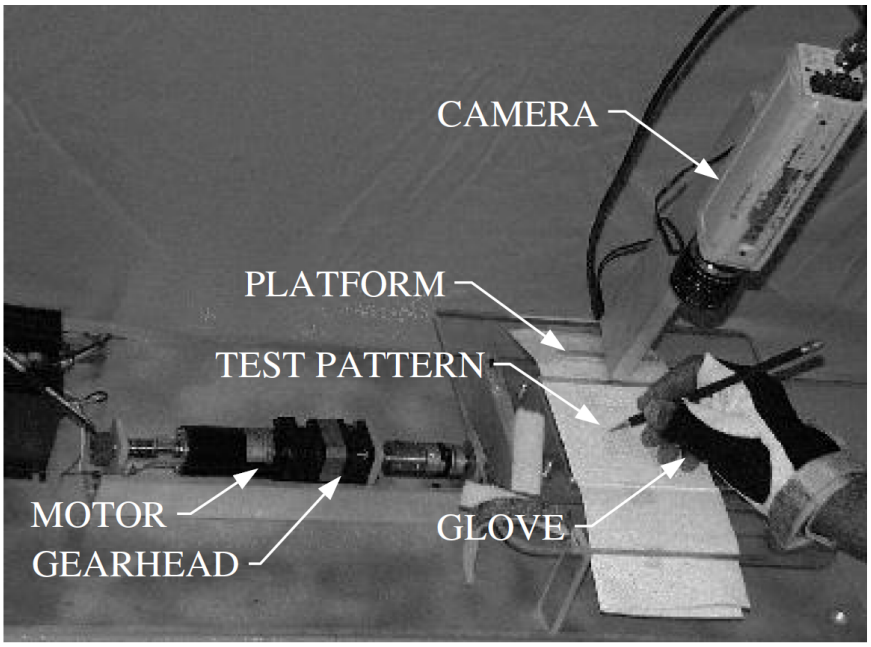

Figure 1.4: Moving platform (source: [Trejos et al., 1999]).

Following the insurgency of MICABG, [Nakamura et al., 2001] proposes a surgical robotic system with heartbeat synchronization for beating heart surgery. The robotic system provides the illusion of a motionless heart by cancelling relative motion between the heart and the robot end-effector, and providing the surgeon with a stable visual feedback. First, two cameras are responsible for visual stabilization, a monochrome high-speed camera tracks artificial markers on the heart surface to determine displacement information, which is then used in concert with the images captured by a color camera to provide a stabilized target point image. Secondly, the displacement information is used for motion stabilization through which the control architecture synchronizes the slave robot with the heart motion. Finally, the master-slave control transforms the master motion into slave robot movements.

[Ginhoux et al., 2005], based on two different control schemes, presents a predictive-control approach for compensation of physiological motions during beating heart surgery. One control scheme is intended to control respiratory motions through a modified generalized predictive controller (GPC) so it learns the disturbance cycle and, thus, better predict it. This modified GPC, called the R-GPC, allows for a separation of the periodical disturbance-rejection function from the reference-following function. It is assumed that the patient is

under artificial ventilation and thus have a perfectly periodical respiration cycle. On the other hand, the other control scheme attempts to compensate heart motion. Due to the heart motions complexity, an adaptive disturbance predictor is used in combination with a standard GPC. The prediction algorithm uses displacement information in order to predict future disturbance values. The displacement information is obtained by visual tracking of artificial markers placed on the heart.

A model-based intelligent active relative motion cancelling (ARMC) algorithm is proposed in [Bebek and Çavu\Cso\Uglu, 2007]. Information from multiple sensors (displacement information, electrocardiogram, and arterial and ventricular blood pressures) is used in concert with model predictive control to estimate future heartbeat motion. Cardiac and respiratory motions are then separated through a pair of complementary filters. While respiratory motion is cancelled by a simple feedback based controller due to its low frequency nature, the heartbeat motion is estimated by a model-based predictive controller using displacement and electrocardiogram (ECG) information. The feedforward part is then calculated with the signal provided by the heart motion model and the feedback signal is calculated with the direct measurements of heartbeat and respiratory motions. By combining these two parts the robot motion control signal is computed (Figure 1.5). The system adapts to heart cycle rhythm abnormalities and arrhythmias switching to a safer mode of operation.

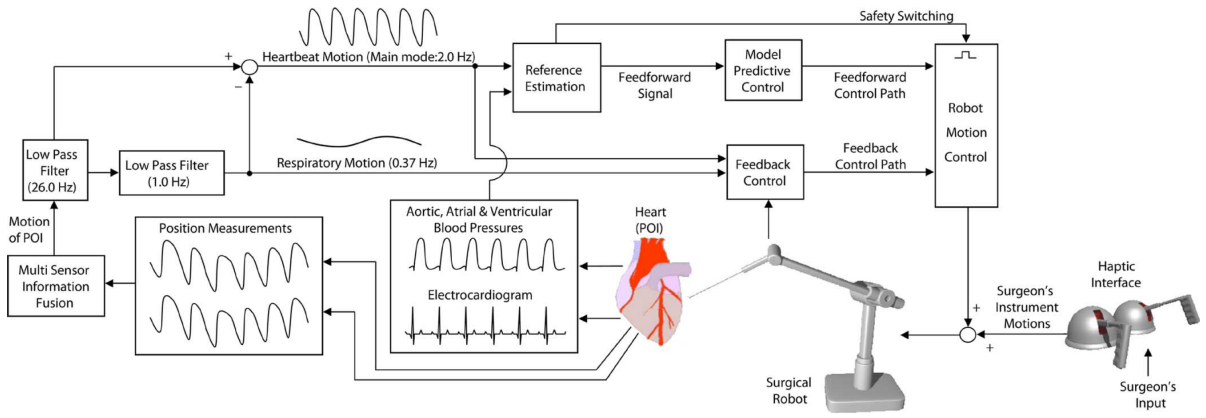

Figure 1.5: Control architecture for ARMC on the beating heart surgery (source: [Bebek and Çavu\Cso\Uglu, 2007]).

Also in the year of 2007, [Cagneau et al., 2007] propose a force feedback control scheme to compensate physiological motions in minimally invasive robotized surgery. The control

scheme uses an outer control loop based in iterative learning control (ILC) coupled with a conventional inner force feedback control loop. The use of ILC allows for control without accurate prediction of the disturbance or an accurate model of the system. Unfortunately, the presented solution is still in its preliminary stages and the results show it is not viable for practical use. Not only does the proposed algorithm suppose that the perturbations are periodic and is only tested for respiratory motions, but also the bad transients during the learning process place unrealistic restrictions. The use of a low-pass filter whose frequency is deduced from discrete wavelet transform (Wavelet Packet Decomposition) is proposed to solve the bad transients but even then the results are far from satisfactory, especially taking into account that compensation capabilities for heart motion are not tested. Even so, Cagneau and co-authors expose the future viability of force control for MICABG.

In [Yuen et al., 2010b] Yuen and co-authors developed a 1 degree-of-freedom (DoF) actuated hand-held device[3], to cancel the 1-D motion component of the mitral valve annulus during beating heart mitral valve annuloplasty. A feed-forward force controller is proposed, using feed-forward heart motion information, determined from a 3-D ultrasound, to overcome the force control bandwidth limitations. In [Yuen et al., 2010a] the MCI is improved to restore force perception. A counterweight moves out of phase with the moving mass of the actuator to negate reaction forces.

Bachta and co-authors in [Bachta et al., 2011] proposed a new active stabilizer with 1 DoF called the Cardiolock 1, which is a piezoactuated compliant mechanism that compensates residual heart motion due to the stabilizer flexibility using vision data. H_∞ control design method is chosen since it allows specification of the stability margins and it has been proven to provide good results with flexible systems. However, it requires prior knowledge of the system parameters and disturbance properties.

Further improving on the idea of an active stabilizer, [Gagne et al., 2012] developed a mechanical system to couple with a classical stabilizer based on a control moment gyroscope to generate the compensation torque, while an accelerometer and an optical sensor measure cardiac motion. The developed system, the GyroLock system, consisting of a gimbal and a gyroscope, is then attached to a standard mechanical stabilizer. Two control approaches are proposed: a Kalman observer base approach, and an adaptive approach. The adaptive approach proved to be a better option mainly due to its tolerance to model uncertainties.

[3]The motion compensation instrument (MCI).

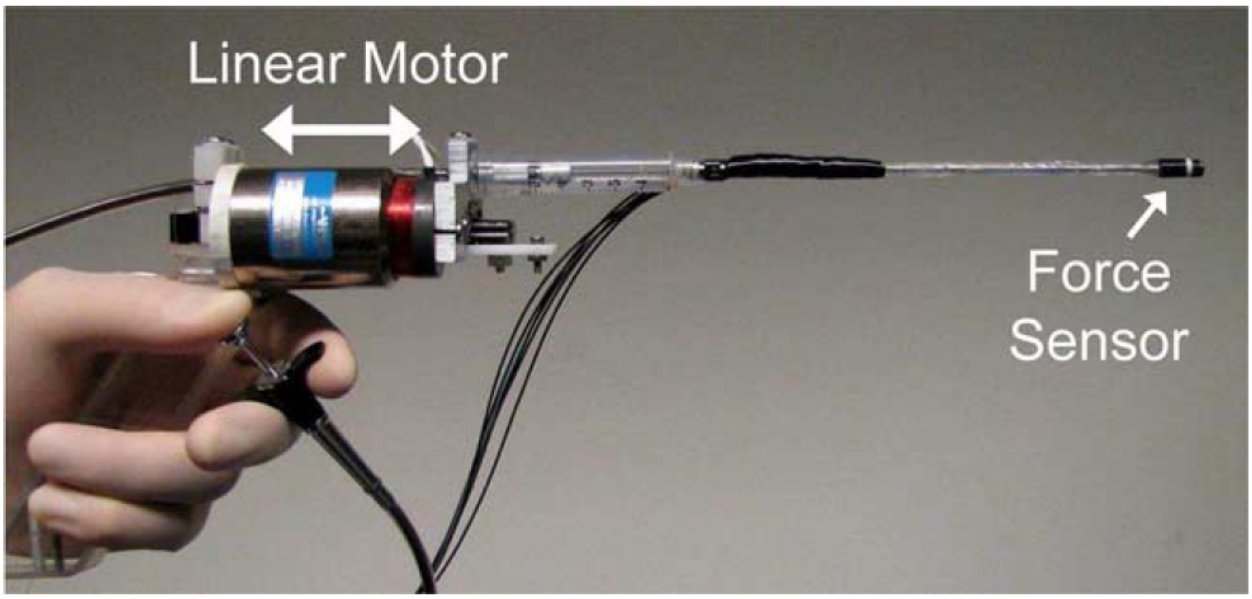

Figure 1.6: The MCI, a hand-held surgical device. It is actuated in 1 degree-of-freedom to cancel the dominant 1-D motion component of the mitral valve annulus. A tip-mounted optical force sensor measures contact forces (source: [Yuen et al., 2010b]).

The *in-vivo* experiment showed promising results however, respiratory motions must be compensated manually and the values obtained are referred to the stabilizer fingers and not the surgeons point-of-interest (the epicardium in this case).

In [Zarrouk et al., 2013] it is proposed a force feedback control architecture composed of two control loops. The inner control loop uses linear state feedback to linearize robot dynamics, and the outer control loop is a 1 DoF PID controller to command the reference force. The controller has been assessed on a experimental platform composed of a Viper robot generating along one axis a sinusoidal motion at 0.125 [Hz] and a D2M2 robot applying a reference force on a piece of foam attached to the Viper robot end-effector.

Khoshnam and Patel [Khoshnam and Patel, 2014] cover the initial steps in designing a motion compensated robotics-assisted catheter manipulation system for conventional steerable ablation catheters. In that regard, a technique for synchronizing the motion of the catheter tip with cardiac motion is used, by estimating the frequency of the heart and reshaping the input trajectory, using vision data. Control capabilities in free space, and contact with static and moving targets are analysed and the limitations of the actuation mechanism are identified. Results show real improvement of the contact force quality, however the actuation mechanism breaks for frequencies superior to 0.65 $[Hz]$ and could not stand the 60 $[s]$ of actuation required for the test.

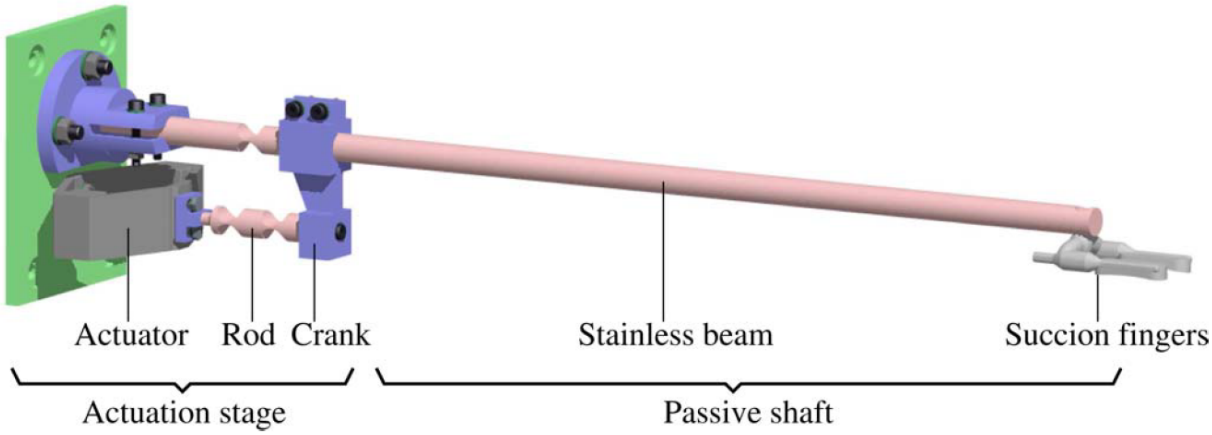

Figure 1.7: Cardiolock 1.

[Kesner and Howe, 2014] presented a catheter robotic system dedicated for beating heart surgery. A custom made integrated force sensing and ablation end effector is used to provide force feedback information. Real time 3-D ultrasound measures target tissue motion to allow synchronisation of the catheter with target motion. Kesner and co-authors proposed force-modulated position controller using force and position feedback to maintain a desired force on a moving target, while compensating for friction and dead zone. Experimental evaluation showed good force control and good compensation capabilities with a force tracking error of 0.11 $[N]$ RMS.

In [Ruszkowski et al., 2015] the *da Vinci* surgical robot heart motion compensation capabilities are tested. In order to do so, an open loop spectral line controller is used to decompose heart trajectory in its spectral components, then the inverse transfer function of the patient side manipulator (PSM) is used at the heart motion spectral frequencies to compute the input that minimizes tracking errors. However, the heart trajectory is assumed to be periodic and known in advance. The results show that the PSM is capable of heart motion compensation with sub-milimetric tracking errors.

[Patronik et al., 2011] further develops on the, previously proposed by the author, robotic device the *HeartLander*, an inchworm-like crawler robot. The *HeartLander* allows for minimally invasive surgery, being inserted into the pericardial sac and adhering to the heart surface, where it moves through suction (Figure 1.8). This device can be used in procedures such as atrial ablation, epicardial electrode placement and myocardial injection of drugs.

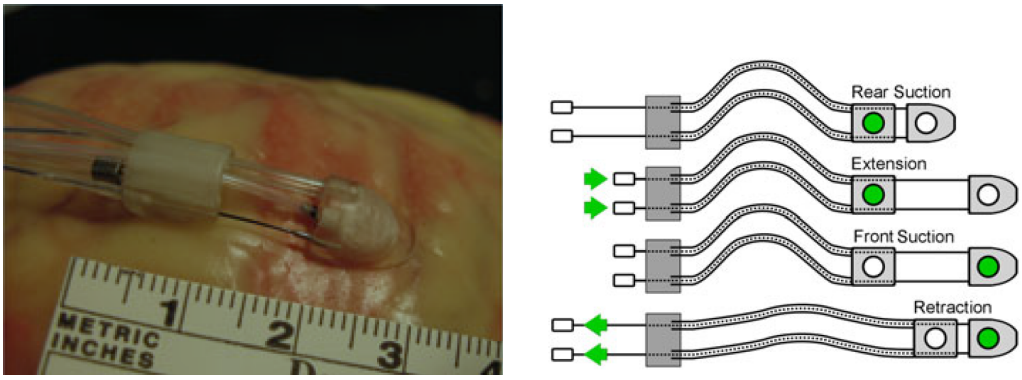

(a) Photograph of the *HeartLander*. (b) *HeartLander* movement cycle.

Figure 1.8: The *HeartLander* (source: [Patronik et al., 2011]).

1.3 Main Objectives and Developed Work

The aim of this thesis is to further develop upon the solution proposed in [Cortesão and Dominici, 2017], a double active observer architecture (AOB) for robotic force control in beating heart surgery. The double AOB architecture consists of two AOB, a type of modified Kalman filter that introduces an extra state to compensate system disturbances. One AOB of order 1 is used for force control, and the second AOB of order 2 compensates physiological motion. This control architecture is capable of high force tracking performance and beating heart motion compensation without the need of *a priori* information of the heart motion. All that is required is a 3-D force sensor at the end-effector to measure contact forces.

The results shown in [Cortesão and Dominici, 2017] were obtained in an *ex vivo* setup without ever having been tested in a simulated environment. Thereunto, the double AOB architecture is implemented in a simulator using C++. The need for this implementation arises from the liberty and confidence it confers in the developing and testing stages, since there is no risk of damaging the manipulator. This simulator consists of a previously developed model of the WAM robot used in [Cortesão and Dominici, 2017], which was developed with recourse to CMake, and is capable of online graphic representation of the robot position, through the use of openGL.

For validity of the work developed and the results exposed in this thesis, it is mandatory that the simulator reliability is proved (i.e. that the WAM model used corresponds to real life behaviour). For this purpose the experimental setup used in [Cortesão and Dominici, 2017] is replicated, and the results obtained in the simulator are compared to those obtained

in *ex vivo* experiments shown in [Cortesão and Dominici, 2017].

Posteriorly, we aim to prove that the double AOB architecture is capable of telemanipulation with haptic feedback. Thus, the double AOB is modified to accommodate telemanipulation. Tests are conducted using 6 DoF haptic device used as the master station, for different control parameters and the results are discussed. Lastly, we ensure the control architecture allows for free-space operation and transitions between contact and free-space.

1.4 Thesis Framework

This thesis follows a simple division in four chapters in order to expose, explain and discuss the main points of focus and the results obtained.

The first chapter motivates the theme and exposes a chronological evolution of the scientific work developed and some of the related contributions to robotic assisted surgery and cardiac surgery. A brief description of the solution proposed is also presented.

The second chapter focuses on explaining the control architecture used for force control, proves its viability and successful implementation in a simulated robot and environment. The results obtained are compared to those previously obtained in [Cortesão and Dominici, 2017] and critically discussed, with the intent to reinforce the possible practical applications of the proposed solution.

The third chapter covers two major components of telemanipulation. First, the force feedback control capabilities of the double AOB architecture coupled with master-slave telemanipulation in constant contact with a stiff environment are tested. Secondly, free-space to contact control transitions are implemented and system performance is tested.

The last chapter concludes the thesis and proposes further improvements to be implemented.

2 System Development

The main goal of this chapter is to validate the simulation of the interaction of a 4 DoF WAM robot with a heart, through comparison of the obtained results to those of [Cortesão and Dominici, 2017] using the same force control architecture and experimental conditions. The control architecture is implemented in the context of robotic assisted beating heart surgery, and its purpose is to compensate 3-D disturbances resulting from breathing and cardiac motion.

2.1 Manipulator Modelling

2.1.1 Manipulator Dynamics

For a set of generalized coordinates q defining the robot's position, the well-known robot dynamics is defined by

$$M(q)\ddot{q} + \upsilon(q, \dot{q}) + g(q) = \tau \tag{2.1}$$

where $M(q)$ is the mass matrix, $\upsilon(q, \dot{q})$ is the vector of Coriolis and centripetal forces, $g(q)$ is the gravity term, and τ is the generalized joint torque. Knowing $\tau = \tau_c - \tau_e - \tau_f$ which are the command, interaction and friction torques, respectively, and considering the friction torque negligible ($\tau_f \approx 0$), then 2.1 can be represented in Cartesian space as

$$\Lambda\ddot{X} + V_x(q, \dot{q}) + g_x(q) = F_c - F_e \tag{2.2}$$

with,

$$\Lambda = J^{-T} M J^{-1}, \tag{2.3}$$

$$\dot{X} = J\dot{q}, \tag{2.4}$$

$$\ddot{X} = J\ddot{q} + \dot{J}\dot{q}, \tag{2.5}$$

$$V_x = J^{-T}\upsilon(q, \dot{q}) - \Lambda\dot{J}\dot{q}, \tag{2.6}$$

$$g_x = J^{-T}g(q), \tag{2.7}$$

and

$$\tau = J^T F \tag{2.8}$$

where J, X, F_c, and F_e are, respectively, the Jacobian matrix, the Cartisian position, the Cartisian force at the end-effector, and the interaction force [Khatib, 1987].

2.1.2 System Model

To achieve a decoupled and linearized system we define F_c as follows

$$F_c = \hat{F}_e + \hat{V}_x(q, \dot{q}) + \hat{g}_x(q) + \hat{\Lambda}f^\star \tag{2.9}$$

where $\hat{F}_e$ is the interaction force estimation and $\hat{V}_x$, $\hat{g}_x$, and $\hat{\Lambda}$ are computed for the given WAM manipulator. Substituting 2.2 in 2.9 we obtain the second order system

$$\ddot{X} = f^\star \tag{2.10}$$

with $f^\star$ as our control input parameter. Assuming a spring contact represented by the environment stiffness K_s, adding a damping loop to the system with gain K_2 to assure a damped Cartesian response, and accounting for the system time delay T_d (mainly due to processing time) we achieve the following system open-loop transfer function

$$G_{ol} = \frac{K_s e^{-sT_d}}{s(s + K_2 e^{-sTd})}, \tag{2.11}$$

which for small T_d can be approximated as

$$G_{ol} = \frac{K_s e^{-sT_d}}{s(s + K_2)}. \tag{2.12}$$

Equation 2.12 can then be represented in temporal domain as

$$\ddot{y}(t) + K_2\dot{y}(t) = K_s u(t - T_d) \tag{2.13}$$

where $y(t)$ is the system output equivalent to the force applied on the environment along one Cartisian direction, and $u(t)$ is the delayed command vector. We can represent 2.13 in state space by defining the two state space variables $x_1 = y(t)$ and $x_2 = \dot{y}(t)$ such that

$$\begin{bmatrix} \dot{x}_1(t) \\ \dot{x}_2(t) \end{bmatrix} = \begin{bmatrix} 0 & 1 \\ 0 & -K_2 \end{bmatrix} \begin{bmatrix} x_1(t) \\ x_2(t) \end{bmatrix} + \begin{bmatrix} 0 \\ K_s \end{bmatrix} u(t - T_d). \tag{2.14}$$

Discretizing with sampling time h [Åström and Wittenmark, 1997], we obtain the following discrete time system

$$\begin{cases} x_{r,k} &= \Phi_r x_{r,k-1} + \Gamma_r u_{k-1} \\ y_k &= C_r x_{r,k} \end{cases} \tag{2.15}$$

$x_{r,k}$ is a three dimensional vector composed by the end-effector force (first state), its derivative (second state), and u_{k-1} (third state), as a consequence of the system time delay $T_d = h$. Equation 2.15 is the open-loop representation of the WAM robotic system and will be used by both AOB as detailed in the next section.

2.2 Double Active Observer

Based on [Cortesão, 2002] and [Cortesão, 2007], a linear system represented in state space by 2.15 can be controlled by state feedback, however 2.15 is not an exact representation of the real system. Unmodeled terms, including noise, higher order dynamics and parameter mismatches, are not tackled in the model design. The AOB addresses this problem by fitting the system input/output behaviour into a linear mathematical model. For this the Kalman filter is reformulated to accommodate an extra state in order to compensate system disturbances. This double AOB architecture allows for a decoupled design for force control and motion compensation. One AOB of order one, which will be referred to as AOB-1 throughout this thesis, is responsible for guaranteeing a desired closed loop dynamic for force control. The second AOB, which will be referred to as AOB-2, is of order two and controls physiological motion compensation.

2.2.1 AOB Structure

For a system defined by

$$\begin{cases} x_{r,k} &= \Phi_r x_{r,k-1} + \Gamma_r u_{k-1} + \xi_{x_{r,k}} \\ y_k &= C_r x_{r,k} + \eta_k \end{cases} \tag{2.16}$$

an observer of the state $x_{r,k}$, $\hat{x}_{r,k}$ can be defined as such

$$\hat{x}_{r,k} = \Phi_{r,n}\hat{x}_{r,k-1} + \Gamma_{r,n}u_{k-1} + K_k[y_k - C_r(\Phi_{r,n}\hat{x}_{r,k-1} + \Gamma_{r,n}u_{k-1})] \tag{2.17}$$

where $\Phi_{r,n}$ and $\Gamma_{r,n}$ are respectively the nominal state transition and command matrices (the ones used in the design). Φ_r and Γ_r are the real matrices, $\xi_{x_{r,k}}$ and η_k are Gaussian random variables referring to the system and measures. For the estimation error

$$e_{r,k} = x_{r,k} - \hat{x}_{r,k}, \tag{2.18}$$

and considering that the nominal matrices are equal to the real matrices, and $\xi_{x_{r,k}}$ and η_k are equal to zero we have

$$e_{r,k} = (\Phi_r - K_k C_r \Phi_r)e_{r,k-1}. \tag{2.19}$$

The error dynamics given by the eigenvalues of $(\Phi_r - K_k C_r \Phi_r)$ are a function of K_k. The Kalman observer computes the best K_k by minimizing the mean square error of the state estimate due to $\xi_{x_{r,k}}$ and η_k. A deterministic description of $e_{r,k}$ is not feasible so a stochastic approach is attempted. Using state feedback, the error enters the system as an additional input

$$p_k = -L_r e_k \tag{2.20}$$

where L_r is the state feedback gain. p_k is called the active state, and is an extra state which describes system disturbances due to modeling errors.

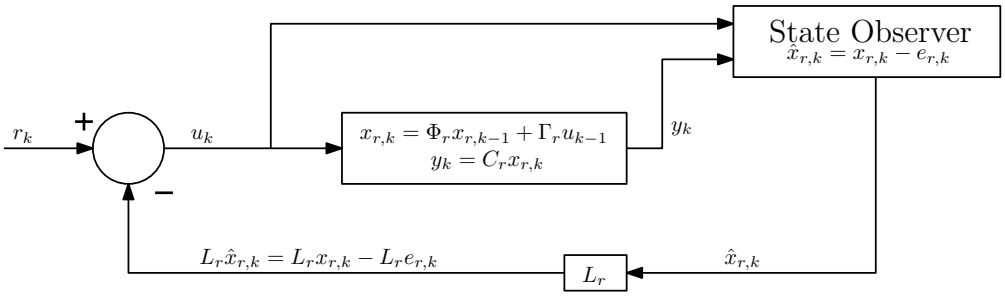

Figure 2.1: State feedback control with classical observer. The observer error $-e_{r,k}$ enters in the system through the state feedback gain L_r.

As seen in Figure 2.1 the error enters the system as an unwanted input which is not visible to the command input u_k. The state space equation must be adapted to accommodate the active state p_k, which leads to an extended state space representation.

In Figure 2.2 the AOB re-injects the active state estimation $\hat{p}_k$ into the control loop, thus compensating the undesired input p_k and ensuring the desired system behaviour.

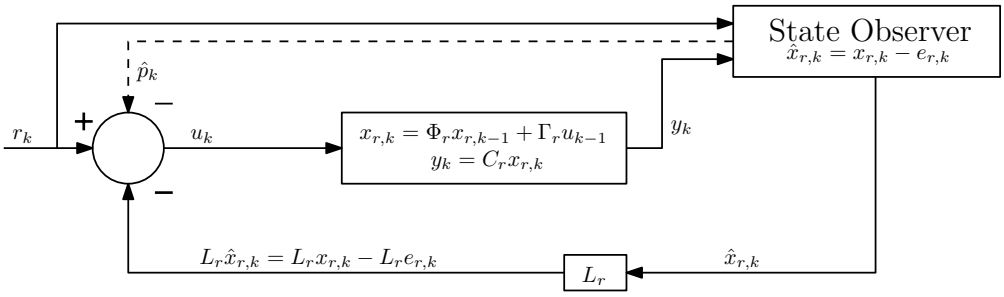

Figure 2.2: State feedback control with AOB. The active state $\hat{p}_k$ is re-injected in the control loop to compensate the error $e_{r,k}$.

The active state p_k has to be able to track a function with unknown dynamics, so a stochastic equation is used to describe it

$$p_k = \sum_{j=1}^{N} (-1)^{j+1} \frac{N!}{j!(N-j)!} p_{k-j} + {}^{N-1}\omega_k \tag{2.21}$$

where ω_k is a Gaussian random variable with zero mean. 2.21 says that the N^{th} order derivative of p_k is randomly distributed. If

$${}^{N-1}\omega_k = 0 \tag{2.22}$$

then 2.21 is a deterministic model for any disturbance p_k that has its N^{th} derivative equal to zero.

For the general case of an AOB of order N (AOB-N), 2.21 has the following state space representation

$${}^{N}p_k = \Phi_{2,2}\, {}^{N}p_{k-1} + {}^{N}\xi_k \tag{2.23}$$

with,

$${}^{N}p_k = \begin{bmatrix} p_{k-(N-1)} & p_{k-(N-2)} & \dots & p_{k-1} & p_k \end{bmatrix}, \tag{2.24}$$

$${}^{N}\xi_k = \begin{bmatrix} 0 & 0 & \dots & 0 & {}^{N-1}\omega_k \end{bmatrix}^T \tag{2.25}$$

and

$$\Phi_{2,2} = \begin{bmatrix} 0 & 1 & 0 & \dots & 0 \\ 0 & 0 & 1 & \dots & 0 \\ \vdots & \vdots & \vdots & \ddots & \vdots \\ 0 & 0 & 0 & \dots & 1 \\ a_N & a_{N-1} & a_{N-2} & \dots & a_1 \end{bmatrix} \tag{2.26}$$

with $a_i = (-1)^{i+1}\frac{N!}{i!(N-i)!}, \quad i = 1, \ldots, N.$

Introducing the extra state p_k and its estimation $\hat{p}_k$ in 2.15, we get the system open loop extended state space equation

$$\begin{bmatrix} {}^{M}x_k \\ {}^{N}p_k \end{bmatrix} = \begin{bmatrix} \Phi_r & \Phi_{1,2} \\ 0 & \Phi_{2,2} \end{bmatrix} \begin{bmatrix} {}^{M}x_{k-1} \\ {}^{N}p_{k-1} \end{bmatrix} + \begin{bmatrix} \Gamma_r \\ 0 \end{bmatrix} u'_{k-1} + \begin{bmatrix} {}^{M}\xi_k \\ {}^{N}\xi_k \end{bmatrix} \tag{2.27}$$

where ${}^{M}\xi_k$ is the uncertainty associated with the state variable ${}^{M}x_k$,

$$u'_{k-1} = r_{k-1} - \begin{bmatrix} L & 1 \end{bmatrix} \begin{bmatrix} {}^{M}\hat{x}_k \\ {}^{N}\hat{p}_k \end{bmatrix}, \tag{2.28}$$

$${}^{M}x_k = \begin{bmatrix} x'_k & u_{k-d} & \ldots & u_{k-2} & u_{k-1} \end{bmatrix} \tag{2.29}$$

and

$$\Phi_{1,2} = \begin{bmatrix} 0 & \ldots & 0 \\ \vdots & \ddots & \vdots \\ 0 & \ldots & 1 \end{bmatrix}. \tag{2.30}$$

For $\hat{p}_k = p_k$ we obtain the desired closed loop system, with the state space representation

$$\begin{bmatrix} {}^{M}x_k \\ {}^{N}p_k \end{bmatrix} = \begin{bmatrix} \Phi_r - \Gamma_r L_r & 0 \\ 0 & \Phi_{2,2} \end{bmatrix} \begin{bmatrix} {}^{M}x_{k-1} \\ {}^{N}p_{k-1} \end{bmatrix} + \begin{bmatrix} \Gamma_r \\ 0 \end{bmatrix} r_{k-1} + \begin{bmatrix} {}^{M}\xi_k \\ {}^{N}\xi_k \end{bmatrix}, \tag{2.31}$$

the control gain L_r can be obtained by Ackermann's formula

$$L = \begin{bmatrix} 0 & \ldots & 0 & 1 \end{bmatrix} W_c^{-1} P(\Phi_r) \tag{2.32}$$

where $W_c = \begin{bmatrix} \Gamma_r & \Phi_r\Gamma_r & \ldots & \Phi_r^{M-1}\Gamma_r \end{bmatrix}$ is the controllability matrix, and $P(\Phi_r)$ is the desired characteristic polynomial.

The state estimation is therefore defined by

$$\begin{aligned} \begin{bmatrix} {}^{M}\hat{x}_k \\ {}^{N}\hat{p}_k \end{bmatrix} &= \begin{bmatrix} \Phi_r - \Gamma_r L_r & 0 \\ 0 & \Phi_{2,2} \end{bmatrix} \begin{bmatrix} {}^{M}\hat{x}_{k-1} \\ {}^{N}\hat{p}_{k-1} \end{bmatrix} + \begin{bmatrix} \Gamma_r \\ 0 \end{bmatrix} r_{k-1} \\ &+ K_k \left\{ y_k - C_a \left(\begin{bmatrix} {}^{M}\hat{x}_k \\ {}^{N}\hat{p}_k \end{bmatrix} = \begin{bmatrix} \Phi_r - \Gamma_r L_r & 0 \\ 0 & \Phi_{2,2} \end{bmatrix} \begin{bmatrix} {}^{M}\hat{x}_{k-1} \\ {}^{N}\hat{p}_{k-1} \end{bmatrix} + \begin{bmatrix} \Gamma_r \\ 0 \end{bmatrix} r_{k-1} \right) \right\}. \end{aligned} \tag{2.33}$$

The Kalman gain K_k is given by

$$K_k = P_{1k} C_a^T \left[C_a P_{1k} C_a^T + R_k \right]^{-1} \tag{2.34}$$

with

$$P_{1k} = \Phi_a P_{k-1} \Phi_a^T + Q_k \tag{2.35}$$

and

$$P_k = P_{1k} - K_k C_a P_{1k}. \tag{2.36}$$

Φ_a is the augmented open loop matrix

$$\Phi_a = \begin{bmatrix} \Phi_r & \Gamma_r \\ 0 & 1 \end{bmatrix} \tag{2.37}$$

and C_a is the augmented measurement matrix

$$C_a = \begin{bmatrix} C_r & 0 \end{bmatrix}. \tag{2.38}$$

Q_k and R_k are the system and measurement noise matrices, respectively. Q_k is of the form

$$Q_k = \begin{bmatrix} Q_{M x_k} & 0 \\ 0 & Q_{N p_k} \end{bmatrix}. \tag{2.39}$$

$Q_{M x_k}$ is a diagonal matrix and its values should be lower than the values of $Q_{N p_k}$ since all system disturbances should be compensated with ${}^N p_k$. P_k is the mean square error matrix and its initial values should not be lower than the initial values of Q_k ($P_0 \geq Q_0$).

The absolute values of Q_k and R_k are not important, only the relative relation between them, since if the values of Q_k, R_k and P_k are all multiplied by the same coefficient the value of K_k remains the same. As such, the values of Q_k and R_k are determined based on the accuracy of the model versus the accuracy of the measures. If the model is very accurate with respect to the measures then $R \gg Q$, which results in low values of K_k. If the contrary is true then $Q \gg R$, and K_k has high values.

2.2.2 AOB-1

An AOB of order N gives the system the capability to track non-linear disturbances but decreases robustness to stiffness mismatches, therefore a AOB of order 1 is used for force control.

As stated above, Lr is determined by Ackermann's formula, such as in 2.32, as to ensure the desired system dynamics, defined by the characteristic polynomial

$$P(z) = z^2 + b_1 z + b_2 \tag{2.40}$$

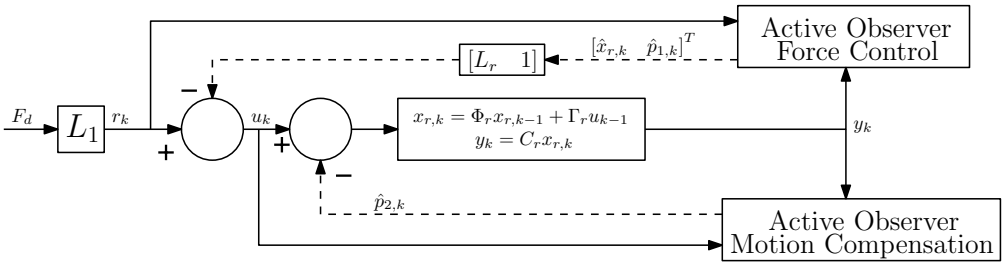

Figure 2.3: Control architecture with double AOB.

with,

$$b_1 = -2e^{-\zeta\omega_n h}\cos(\omega_n\sqrt{1-\zeta^2}h) \tag{2.41}$$

and

$$b_2 = e^{-2\zeta\omega_n h}, \tag{2.42}$$

ζ, ω_n and h being respectively the damping factor, cut-off frequency and sampling time. By 2.21, $p_{1,k}$ is

$$^1p_{1,k} = p_{1,k-1} + {}^0\omega_k \tag{2.43}$$

and

$$\Phi_{2,2} = 1. \tag{2.44}$$

Substituting in 2.33 we have the state representation equation

$$\begin{aligned}\begin{bmatrix}\hat{x}_{r,k}\\ {}^1\hat{p}_{1,k}\end{bmatrix} &= \begin{bmatrix}\Phi_r - \Gamma_r L_r & 0\\ 0 & 1\end{bmatrix}\begin{bmatrix}\hat{x}_{r,k-1}\\ \hat{p}_{1,k-1}\end{bmatrix} + \begin{bmatrix}\Gamma_r\\ 0\end{bmatrix} r_{k-1}\\ &+ K_{1,k}\left\{y_k - C_a\left(\begin{bmatrix}\Phi_r - \Gamma_r L_r & 0\\ 0 & 1\end{bmatrix}\begin{bmatrix}\hat{x}_{r,k-1}\\ \hat{p}_{1,k-1}\end{bmatrix} + \begin{bmatrix}\Gamma_r\\ 0\end{bmatrix} r_{k-1}\right)\right\}\end{aligned} \tag{2.45}$$

2.2.3 AOB-2

Respiratory and heart motions are of periodic nature and can be acceptably described by a second order function, so an AOB of order 2 is used to compensate this physiological motions. Using an AOB only for motion compensation allows for a decoupled motion compensation and force control design. Since the dynamics are enforced by the AOB-1 the control gain L_r for the AOB-2 is zero, therefore, only the active state $p_{2,k}$ is re-injected into the control loop. As the AOB-2 is of order 2 the active state $p_{2,k}$ will have dimension 2 and is defined by

$$^2p_{2,k} = 2p_{2,k-1} - p_{2,k-2} + {}^1\omega_k \tag{2.46}$$

and

$$\Phi_{2,2} = \begin{bmatrix} 0 & 1 \\ -1 & 2 \end{bmatrix}. \tag{2.47}$$

Substituting in 2.33 we have the state representation equation

$$\begin{aligned} \begin{bmatrix} \hat{x}_{r,k} \\ {}^2\hat{p}_{2,k} \end{bmatrix} &= \begin{bmatrix} \Phi_r - \Gamma_r L_r & 0 & 0 \\ 0 & 0 & 1 \\ 0 & -1 & 2 \end{bmatrix} \begin{bmatrix} \hat{x}_{r,k-1} \\ \hat{p}_{2,k-2} \\ \hat{p}_{2,k-1} \end{bmatrix} + \begin{bmatrix} \Gamma_r \\ 0 \\ 0 \end{bmatrix} r_{k-1} \\ &+ K_{2,k} \left\{ y_k - C_a \left(\begin{bmatrix} \Phi_r - \Gamma_r L_r & 0 & 0 \\ 0 & 0 & 1 \\ 0 & -1 & 2 \end{bmatrix} \begin{bmatrix} \hat{x}_{r,k-1} \\ \hat{p}_{2,k-2} \\ \hat{p}_{2,k-1} \end{bmatrix} + \begin{bmatrix} \Gamma_r \\ 0 \\ 0 \end{bmatrix} r_{k-1} \right) \right\} \end{aligned} \tag{2.48}$$

2.2.4 Command Torque

From 2.1, 2.8 and 2.9 we can extract the command torque τ_c equation

$$\tau_c = \upsilon(q, \dot{q}) + g(q) + J^T(q)\Lambda(q)(f^\star - \dot{J}\dot{q}) + \tau_e, \tag{2.49}$$

where τ_e is the interaction torque. $\dot{J}\dot{q}$ results in a high frequency component and is therefore negligible. $f^\star$ is a three dimensional vector for Cartesian control, with each Cartesian dimension $f_i^\star$ defined by

$$f_i^\star = L_1 F_{r,i} - \begin{bmatrix} L_r & 1 \end{bmatrix} \begin{bmatrix} \hat{x}_{r,k} & \hat{p}_{1,k} \end{bmatrix}^T - \hat{p}_{2,k} - K_2 \dot{X}_i. \tag{2.50}$$

The estimates $\hat{x}_{r,k}$, $\hat{p}_{1,k}$ and $\hat{p}_{2,k}$ are computed by the double AOB architecture for each Cartesian dimension, and $f_i^\star$ the corresponding acceleration input.

In Figure 2.4 the resulting double AOB control scheme is represented. It is possible to observe that the effects of τ_e on the robot are compensated by its estimate $\hat{\tau}_e$, and in the case of the simulation this compensation is perfect since the values of $\hat{F}_e$ are not compromised by the limitations of a force sensor.

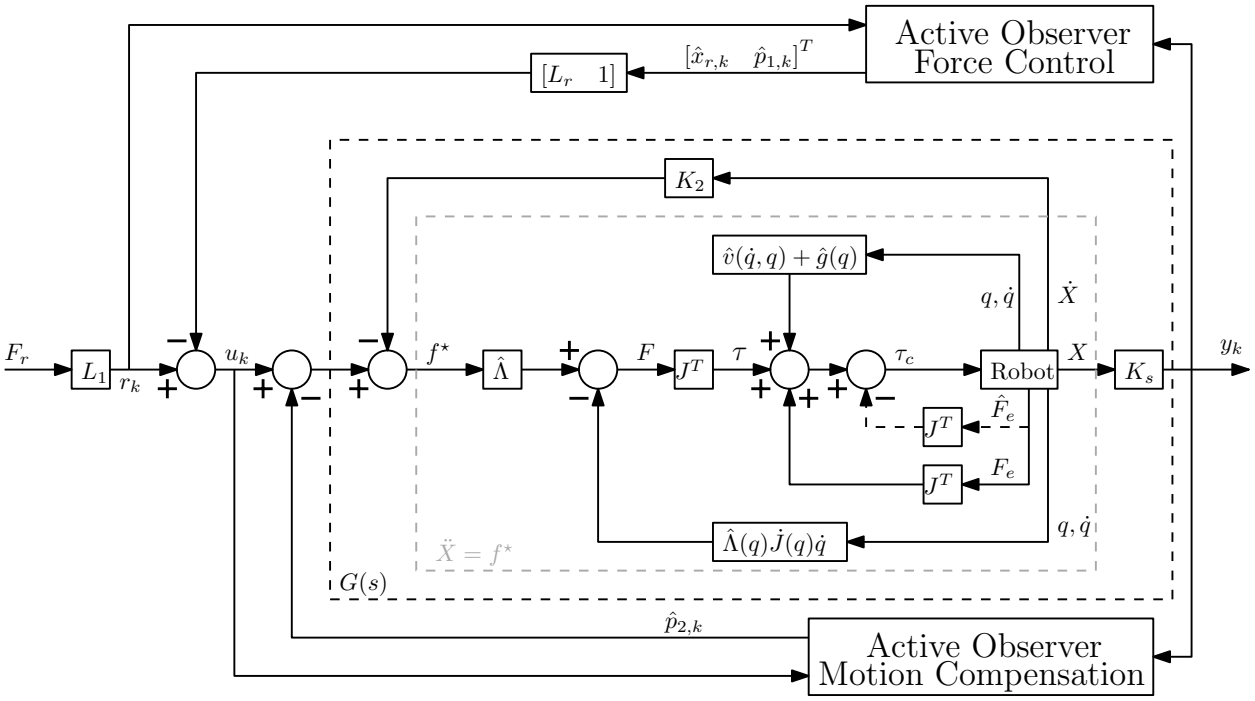

Figure 2.4: Double AOB control scheme for robot force control with compensation for physiological motion. F_r is the reference force tracked by y_k with the desired tracking dynamics. The system plant $G(s)$ is defined by $\ddot{X} = f^\star$, the system stiffness K_s, the damping gain K_2 and the system time delay T_d. F_e is the force exerted in the robot that results from contact with the heart, and $\hat{F}_e$ is its estimation (obtained by a force sensor for example). F_e injects disturbances resultant from heart and breathing motions into the system which are compensated by the active state $p_{2,k}$.

2.3 Software Development

The architecture described in the previous section has never been implemented in a simulated environment, since the results shown in [Cortesão and Dominici, 2017] were obtained in an *ex vivo* setup. There is no doubt that the impact of pratical results is much higher than the impact of their simulated counterparts, however the use of a simulator allows for more liberty and confidence especially in the development stages, since there is no guarantee that a given setup will lead to a stable behaviour. That being said, the implementation of the double AOB architecture in a simulator is an important step to deepen the study of its performance and to allow for easier testing of other solutions in which it may be used.

As such, the double AOB architecture was implemented on a simulated environment using C++. This simulator had been previously developed using CMake and corresponded to a

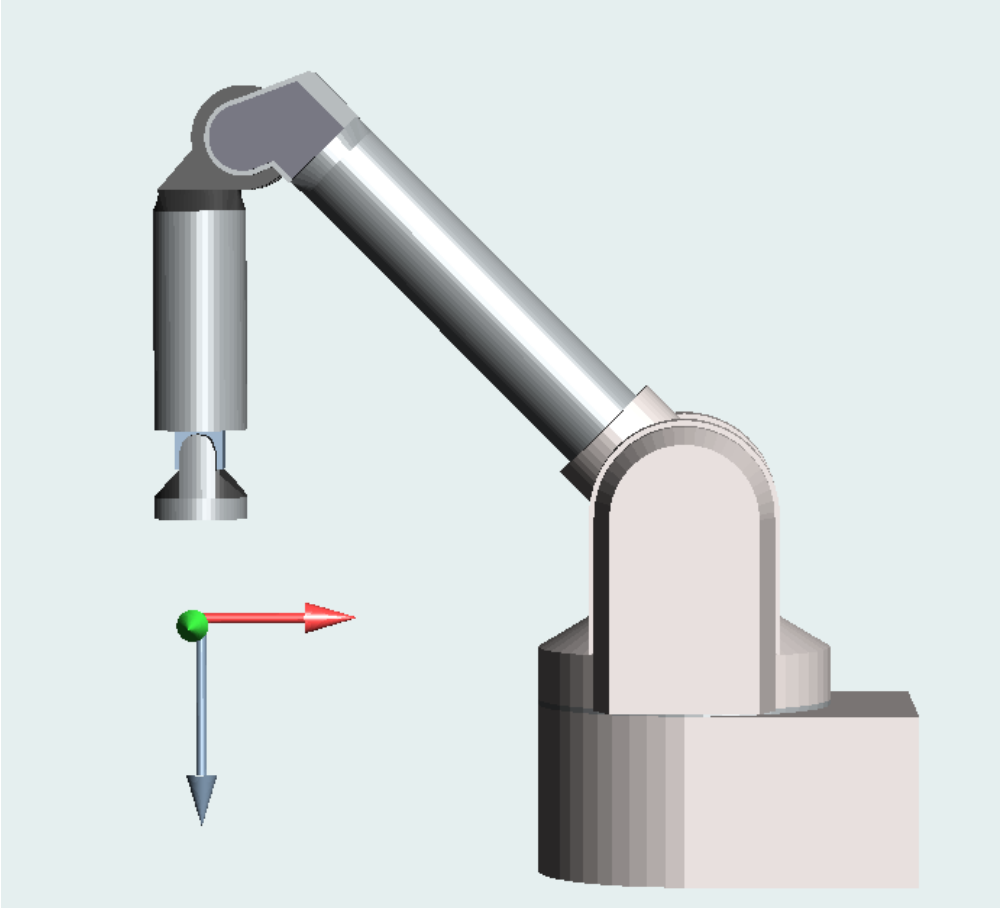

Figure 2.5: WAM robot with axes. The three axes represented in red, green and pale blue are $-X$, $-Y$ and Z respectively.

model of the WAM robot used in [Cortesão and Dominici, 2017]. The simulator is capable of an online graphic representation of the WAM robot position, as shown in Figure 2.5 (where the three axes are represented in red, green and pale blue for $-X$, $-Y$ and Z respectively). C++ is an object oriented programming language, therefore for the implementation of the double AOB we use two classes (objects). One class is the AOB class which holds all the constants and variables relevant to the Active Observers, as well as the functions required to modify its values and update the state estimations $\hat{x}_{r,k}$ and $\hat{p}_k$. The AOB class has a generic constructor which allows for the creation of an Active Observer of order N. The second class is the controller class which will hold two objects of the class AOB, corresponding to the AOB-1 and AOB-2, and all the other variables, constants, and functions needed for force control using the double AOB architecture.

A simple code fluxogram is represented in Figure 2.6. It is worth noting that in the first step of the control loop, the interaction force is determined in a function that simulates

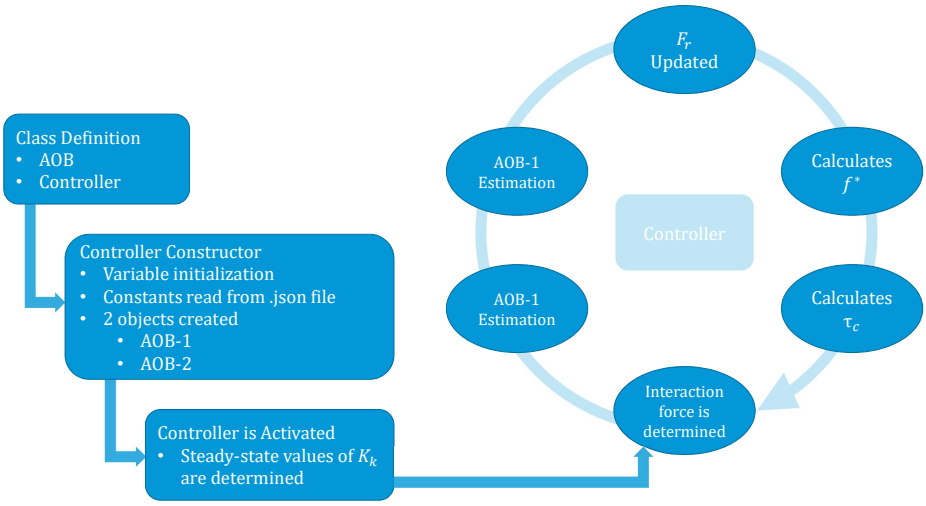

Figure 2.6: Code fluxogram.

the heart surface (with or without physiological motion) through the use of virtual walls. The use of the *.json* file in the Controller class constructor allows for the tweaking of setup and control parameters without the need to recompile all the code. The control loop is programmed in accordance with the control schematic represented in Figure 2.4.

All the tests and simulations were performed in a 2.9 GHz Intel Core i7-7500U running Ubuntu 16.04.

2.4 Validation in a Simulated Environment

In this section we aim to validate the simulator used through the comparison of the results obtained in [Cortesão and Dominici, 2017] with the results obtained in the simulator after replicating the experimental setup. For that purpose, the parameters for the double AOB architecture and for the simulation are defined, according to those used in [Cortesão and Dominici, 2017]. The breathing and heart motions are reproduced by a function that generates virtual walls (representing the heart surface) for each Cartesian direction and, simulates the corresponding displacements based on physiological data obtained from *in-vivo* experiments on a pig's heart [Sauvée et al., 2007]. The function then returns the contact force the

simulated heart exerts on the robot end-effector for a heart stiffness of

$$K_s = 810[N/m]. \tag{2.51}$$

In contrast, our system (defined in 2.14) has the environment stiffness estimation

$$\hat{K}_s = 900[N/m], \tag{2.52}$$

the damping coefficient

$$K_2 = 10, \tag{2.53}$$

and a time delay T_d equal to the sampling time $h = 1[ms]$.

Therefore, for a critically damped force control ($\zeta = 1$) with time constant equal to $3[ms]$, we have the state feedback gain L_r

$$L_r = \begin{bmatrix} 89.7299 & 0.6606 & 0.5570 \end{bmatrix} \tag{2.54}$$

.

AOB-1 Parameters

For the force control loop, R_k is set to 1 and Q_k is a $4x4$ matrix defined by

$$Q_{x_k} = \begin{bmatrix} 10^{-12} & 0 & 0 \\ 0 & 10^{-12} & 0 \\ 0 & 0 & 10^{-12} \end{bmatrix} \tag{2.55}$$

and

$$Q_{p_{1,k}} = 0.5, \tag{2.56}$$

which leads to the steady-state AOB gain

$$K_{1,k} = \begin{bmatrix} 0.1499 & 12.1672 & 0.6520 & 0.6520 \end{bmatrix}^T. \tag{2.57}$$

AOB-2 Parameters

For motion compensation, R_k is set to 1 and Q_k is a $5x5$ matrix defined by

$$Q_{p_{1,k}} = \begin{bmatrix} 0 & 0 \\ 0 & 5 \end{bmatrix} \tag{2.58}$$

and Q_{x_k} is equal to 2.53. This gives us the steady-state AOB gain

$$K_{2,k} = \begin{bmatrix} 0.4194 & 113.3134 & 21.9619 & 21.9619 & 23.6657 \end{bmatrix}^T. \tag{2.59}$$

Simulation Setting

The objective of this experiment is to assess the control capabilities of the double AOB architecture. As such, the simulated WAM robot exerts three-dimensional forces on the virtual walls that simulate the heart, under displacements associated with breathing and heartbeat. With the intent to simulate a simple surgical task, the desired reference force F_r is zero along the X and Y and time varying only along the Z axis. The reference force is composed of ramps, constants and an up-chirp signal from $0.2[Hz]$ to $1[Hz]$, as to simulate compression, decompression, and harmonic excitation on the heart surface. F_r begins at $2[s]$ and lasts for $35[s]$. The physiological motions begin at $7[s]$, last for $15.2[s]$, are interrupted for $1[s]$, and then repeat for another $15.2[s]$.

For analysis purposes, such as in Cortesão and Dominici, two different experimental datasets are obtained. One dataset is obtained with constant virtual walls, i.e. no displacements through time with the intent to simulate a motionless heart, to obtain the measured force resulting from the correspondent reference force alone. The second dataset is obtained with recourse to the physiological data referred above, in order to register the measured force resulting from reference force and motion compensation. It is noteworthy that no perforation of the heart surface occurs in Cortesão and Dominici and, therefore, it is also not simulated here.

2.5 Results and Discussion

In this section it is possible to evaluate the control capabilities of the double AOB architecture in the presence of physiological motion and stiffness mismatches. The power spectral density plot (PSD) of the disturbance forces is depicted in Figure 2.7. The force control results are observable in Figure 2.8, where F_r is represented in black, and the measured forces are represented in blue, green and red for X, Y and Z axes respectively. Partial root mean square errors for the X, Y and Z axes are shown in table 2.1, for different types of robot motion. As can be seen in the PSD plot, the relevant heartbeat components are the main one and the first harmonic at around 1.2 $[Hz]$ and 2.4 $[Hz]$ respectively. In both the X and Y axis the controller performs better under physiological motions (Figure 2.8 (c) and (d) and Table 2.1) mostly because of the "valley" effect mentioned in [Cortesão and Dominici, 2017] which creates an adverse effect since the controller attempts to achieve 0 $[N]$ for all

lateral forces. This effect is pronounced when the reference force is constant. Error along Z is higher under physiological motions when compared to the X and Y axes mainly due to a much higher respiration activity along the Z axis, as seen in Figure 2.7, and also due to the varying force reference. Nevertheless, the results obtained are highly positive with an average RMSE along Z of approximately 0.1148 $[N]$ which corresponds to a displacement of approximately 0.1417 $[mm]$, and also sub-milimetric errors along X and Y.

The shown results prove that the double AOB architecture as been successfully implemented in the simulator, and that the simulated WAM robot and environment behave accordingly to real life standards. The overall performance of the controller is superior to the one achieved in [Cortesão and Dominici, 2017] as is to be expected, since real life experiments entail higher model uncertainties and disturbances. The purpose of this chapter has been achieved providing a platform upon which to study and expand the proposed control architecture as shown in the next chapter.

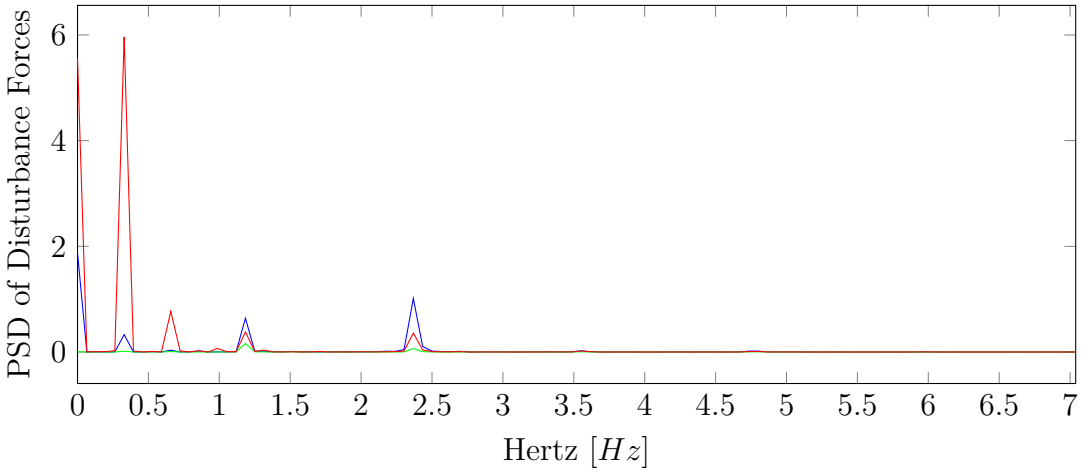

Figure 2.7: Power spectral density (PSD) of the disturbance forces due to physiological motions. Represented in blue, green and red are the X, Y and Z axes, respectively.

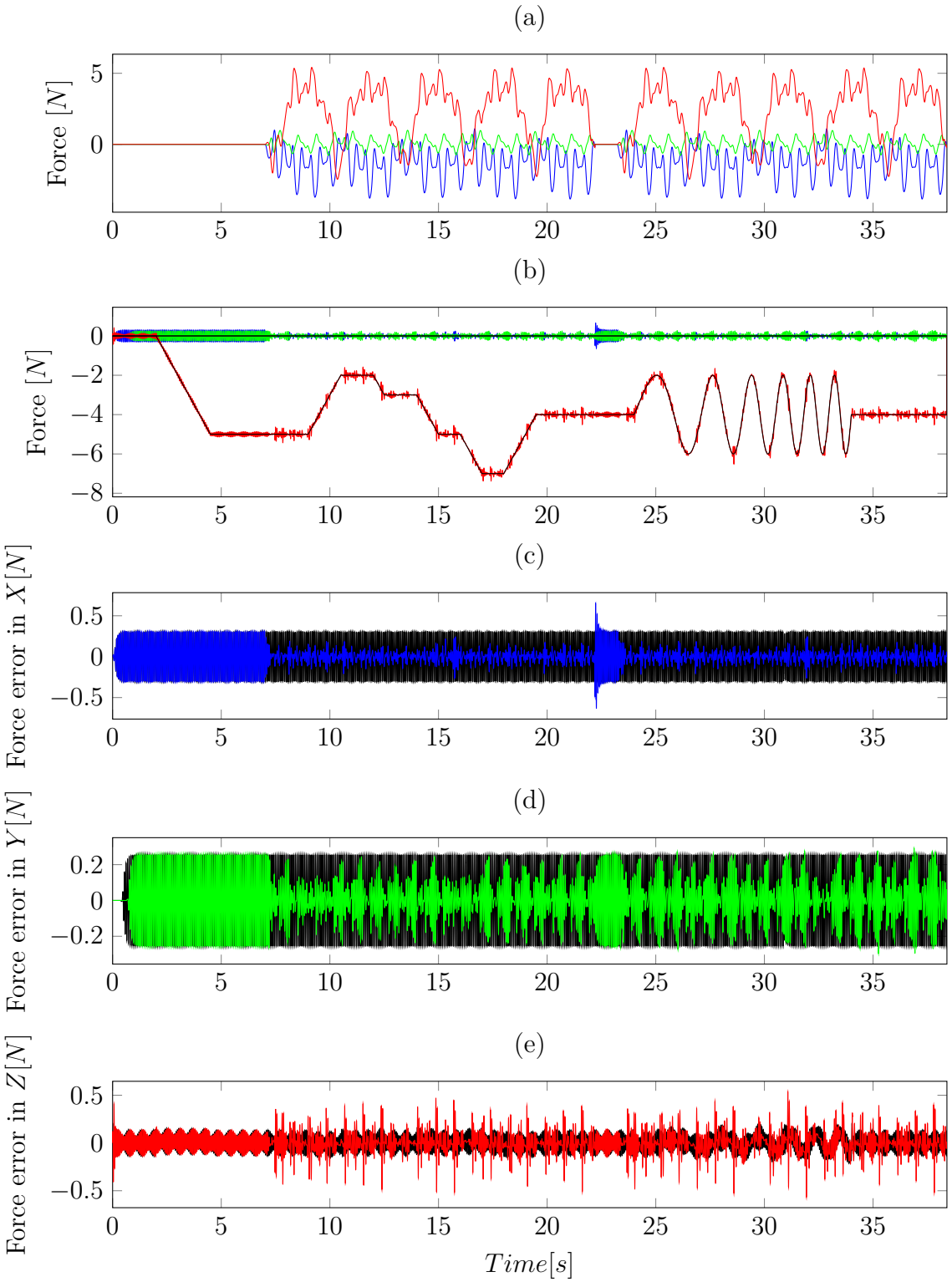

Figure 2.8: Experimental results obtained for double AOB force control. X, Y and Z are represented in blue, green and red, respectively. (a) Disturbance forces referred to the contact point. (b) Three dimensional reference force Fr is represented in black.(c), (d) and (e) Force errors with physiological motion (colored plots) and without physiological motion (black plots).

Table 2.1: RMSE of the force. Bold values represent error in the presence of physiological motion and non bold values represent error without physiological motion.

	Compression	Constant Force	Releasing	Harmonic Excitation
Time $[s]$	[12-12.5] [14-15] [16-17]	[7-9];[10.5-12];[12.5-14] [15-16];[17-18] [19.5-22.2];[23.2-24];[34-38]	[9-10.5] [18-19.5]	[24-34]
X axis $[N]$	**0.0592** 0.2104	**0.1001** 0.2106	**0.0624** 0.2106	**0.0632** 0.2104
Y axis $[N]$	**0.0899** 0.1762	**0.1169** 0.1764	**0.0898** 0.1758	**0.1047** 0.1760
Z axis $[N]$	**0.1293** 0.0779	**0.1111** 0.0765	**0.1233** 0.0774	**0.1292** 0.0886

3 Telemanipulation

In this chapter, the aim is to improve upon the control architecture exposed in Chapter 2 by implementing telemanipulation capabilities with haptic feedback in the system. This means that a human will operate a master arm in order to carry out the surgical task and the robot (which is the slave) will not only perform the task instructed by the human operator but also feedback information of position and force, thus allowing for augmented operability. In the first part of this chapter we explain the telemanipulation control architecture design, for contact only, and test its capabilities with resort to the *PHANTOM Omni*[1]. On the second part of this chapter we attempt to modify the double AOB to allow for free-space operation and free-space to stiff contact transitions. Telemanipulation is an important step towards an end-user application, and will hopefully allow for the use of this technique in actual surgery.

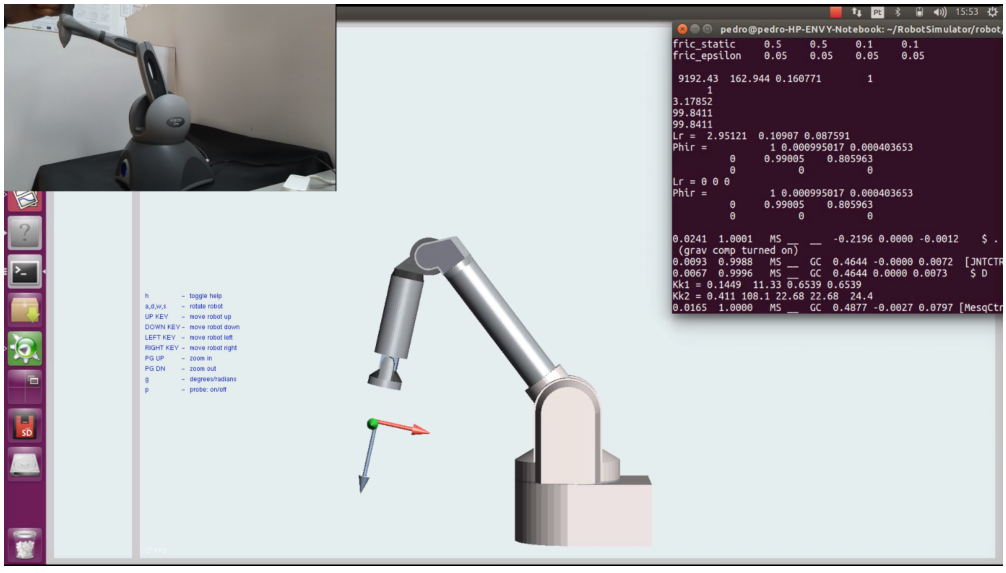

Figure 3.1: Simulation workspace.

The simulator used is the same used in Chapter 2, and the code follows the same scheme as the one represented in Figure 2.6. The simulation workspace is visible in Figure 3.1,

[1]The *PHANTOM Omni* is a 6 degree-of-freedom haptic device by SENSABLE.

where on the left we have the master station, the *PHANTOM Omni*, on the right the console running the code and in the middle the graphic representation of the WAM robot. It is also visible that since the master station is in an elevated position, then the WAM robot is also slightly elevated (movement along the Z axis). All the tests and simulations were once again performed in a 2.9 GHz Intel Core i7-7500U running Ubuntu 16.04.

3.1 Telemanipulation in Contact

3.1.1 Telemanipulation Scheme

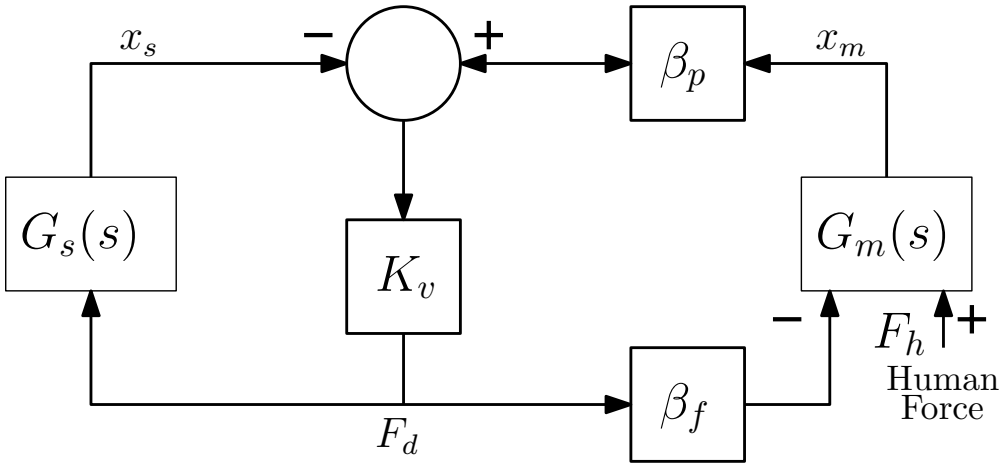

Figure 3.2: Telemanipulation scheme. $G_s(s)$ corresponds to the WAM robot, the double AOB and the environment. $G_m(s)$ corresponds to the haptic device and the human arm.

Figure 3.2 represents the telemanipulation scheme for each cartesian direction with x_m the master position, x_s the slave position, β_p the position scaling and β_f the force scaling. $G_s(s)$ corresponds to the slave station, including the WAM robot, the double AOB and the environment. $G_m(s)$ corresponds to the master station, including haptic device and the human arm. It can be represented by

$$G_m(s) = \frac{1}{m_m s^2 + c_m s + K_m} \tag{3.1}$$

with m_m, c_m and K_m the mass, damping and stiffness of the master station, respectively.

This telemanipulation scheme is similar to a position-position control scheme but, since the double AOB is a force control architecture, a virtual coupling K_v is added to generate the desired force F_d which will be proportional to the position error between the master and

slave stations. The force control loop of the double AOB architecture will ensure that the slave device tracks the desired force F_d for the established dynamics.

3.1.2 Parameters Tuning

To test the telemanipulation capabilities of the double AOB architecture and tune its parameters two sets of experiments are conducted, one without physiological motions and one in the presence of physiological motions. Simple low frequency and high amplitude motions are executed along the X axis, then the Y axis, then the Z axis, followed by high frequency and high amplitude motions on the three axes in the same order, and finally motions along all three axis simultaneously. Physiological motions are once again introduced at $7[s]$, last for $15.2[s]$ where the low frequency and high amplitude motions are executed, are interrupted for $1[s]$, and then repeat for another $15.2[s]$ where the remaining movements are executed.

Determining Time Constant

For telemanipulation a time constant $T_c = 3[ms]$ is no longer viable since the system is not stable. Therefore, for each set of experiments (heart off and heart on), performance is tested for different values of T_c varying from $10[ms]$ to $35[ms]$ at fixed intervals of $5[ms]$. Lower time constants introduced too much instability in the system and higher time constants implied too great of a loss in precision and, as such, were deemed not relevant. The following results are obtained for a virtual coupling constant $K_v = 1000$.

The results obtained are shown in Figures 3.3 to 3.9. In Figures 3.3 and 3.4 we compare both extremes of the tested T_c, and a close up is shown in Figure 3.5. From this three figures it is already discernible the consequences of different values of T_c in the system behaviour. For lower time constants there is better tracking of the reference force but higher oscillation of the end-effector occurs. This effect is again due to the "valley" effect[2], that is amplified due to the virtual coupling constant K_v. This oscillation effect is highlighted in Figures 3.6 to 3.9, where the generated reference force is compared to an ideal reference force[3].

[2]As a reminder, the "valley" effect is the deformation of tissue around the end-effector which results in constant lateral force being exerted in the end-effector. This causes the controller to constantly try to negate them and therefore lead to oscillation in the end-effector.

[3]Please note that the ideal reference force is hypothetical, and is obtained by scaling the position reference to fit the generated reference force. It is merely meant to serve as a guide for what is to be expected of a perfectly generated reference force without any oscillation.

Cross referencing this observations with the RMSE shown in Table 3.1 it is now evident that a compromise between tracking error and stability (precision and accuracy) must be made. Considering that for surgical applications stability of the system is of the utmost importance, the results obtained for $T_c = 20$ are the most satisfactory with the lowest force tracking RMSE values while maintaining sub-milimetric accuracy for all three axes[4].

After determining the time constant that generates the most suitable system dynamics, further tests are conducted to determine the effects of different values of K_v on the system.

Table 3.1: RMSE of the force for different values of T_c. Bold values represent error in the presence of physiological motion and non bold values represent error without physiological motion. Values between brackets represent the reference error in relation to an ideal reference.

	$T_c = 10$	$T_c = 15$	$T_c = 20$	$T_c = 25$	$T_c = 30$	$T_c = 35$
	2.9277	**3.2587**	**3.9090**	**4.8080**	**5.7536**	**6.7122**
X axis $[N]$	2.5142	2.4103	2.6513	3.1455	3.7051	4.2926
	[1.2504]	[0.8350]	[0.5692]	[0.4110]	[0.3215]	[0.2660]
	5.7333	**2.8821**	**2.7941**	**3.3453**	**3.9329**	**4.5594**
Y axis $[N]$	4.7782	2.7107	2.6503	3.1398	3.6988	4.2849
	[2.6128]	[1.0501]	[0.5533]	[0.3695]	[0.2794]	[0.2142]
	1.8529	**2.6173**	**3.4049**	**4.2049**	**5.0095**	**5.8111**
Z axis $[N]$	1.3900	1.9273	2.4979	3.0869	3.6826	4.2826
	[0.2532]	[0.2193]	[0.1815]	[0.1563]	[0.1225]	[0.1122]

Determining K_v

Robustness to stiffness mismatches is not the focus of this section, but to test the telemanipulation capabilities of the double AOB control scheme with haptic feedback[5]. Therefore a perfect estimation of the heart stiffness is assumed (i.e. $K_{s,n} = K_s = 810[N/m]$). Reminiscing to Figure 3.2, it is visible that the value of K_v influences the magnitude of the desired

[4]Accuracy is represented by the RMSE values between brackets in Table 3.1. These values are obtained by calculating the RMSE of the generated reference force for all the instants in time when it should be equal to 0 $[N]$.

[5]For robustness of the AOB architecture to stiffness mismatches consult [Cortesão et al., 2006].

force. So, as seen in Figures 3.10 to 3.13, higher values of K_v entail higher applied forces and consequently better tracking of the master station position, as opposed to lower values of K_v. However, as shown in Figure 3.12, higher values of K_v also entail lower system stability. It is evident by how the desired force oscillations are visible with $K_v = 1600[N/m]$. On the other hand, if the magnitude of oscillations were the same with $K_v = 100[N/m]$ then it would be even more evident, given that the scale is much smaller.

This observation is further reinforced by Table 3.2, which shows the RMSE associated with the different values of K_v. Accuracy increases with the decrease of K_v (i.e. the system stability increases). It is also observable that the RMSE decreases with the decrease of K_v. However, the objective is to obtain telemanipulation with haptic feedback and to achieve telepresence $K_v \gg K_{s,n}$, otherwise the user only feels K_v [Cortesão et al., 2006]. Therefore, a compromise must be made between telepresence and overall system performance. As such, a value of $K_v = 1000[N/m]$ is chosen as the desired coupling constant. The choice of this value is also due to mechanical limitations of the master station, the *PHANTOM Omni*, since no increase in telepresence occurred for higher values of K_v.

So, for the control parameters $K_{s,n} = 810[N/m]$, $K_v = 1000[N/m]$, and for a critically damped force control with time constant equal to 20 $[ms]$ the obtained state feedback gain L_r is

$$L_r = \begin{bmatrix} 2.9512 & 0.1091 & 0.0876 \end{bmatrix} \tag{3.2}$$

and the steady-state AOB gains

$$K_{1,k} = \begin{bmatrix} 0.1449 & 11.33 & 0.6539 & 0.6539 \end{bmatrix}^T \tag{3.3}$$

and

$$K_{2,k} = \begin{bmatrix} 0.411 & 108.1 & 22.68 & 22.68 & 24.4 \end{bmatrix}^T . \tag{3.4}$$

3.1.3 Results and Discussion

The results obtained show that the double AOB architecture is capable of telemanipulation capabilities with haptic feedback. For the chosen parameters of $T_c = 20[ms]$ and $K_v = 1000[N/m]$ we have satisfactory system stability, with the highest RMSE being along X and with only $0.3785[N]$ which corresponds to sub-milimetric oscillations around the expect position. However, the precision of the system is compromised in comparison to the performance obtained in Chapter 2, with the RMSE along Z of $3.3987[N]$ (or 4.2 $[mm]$).

Table 3.2: RMSE of the force for different values of K_v. Bold values represent error in the presence of physiological motion and non bold values represent error without physiological motion. Values between brackets represent the reference error in relation to an ideal reference.

	$K_v = 100$	$K_v = 500$	$K_v = 810$	$K_v = 1000$	$K_v = 1200$	$K_v = 1600$
	0.7507	**2.6235**	**3.4817**	**3.8724**	**4.2166**	**4.7794**
X axis $[N]$	0.5057	1.7211	2.2878	2.5559	2.8150	3.2879
	[0.0217]	[0.1388]	[0.2723]	[0.3785]	[0.5178]	[0.8861]
	0.5259	**1.8145**	**2.4395**	**2.7418**	**3.0062**	**3.5269**
Y axis $[N]$	0.4972	1.7136	2.2853	2.5479	2.8027	3.3387
	[0.0186]	[0.1221]	[0.2468]	[0.3382]	[0.4773]	[0.9306]
	0.6681	**2.2992**	**3.0535**	**3.3987**	**3.6988**	**4.1493**
Z axis $[N]$	0.4845	1.6995	2.2455	2.4917	2.7031	3.0308
	[0.0158]	[0.0657]	[0.1017]	[0.1225]	[0.1640]	[0.2560]

This is to be expected from the variation in the time constant that entails a slower response from the system.

Simulated perforation of the heart was attempted. This was achieved by lowering the heart stiffness after a certain threshold of exerted force is achieved, which was then maintained constant until the surgical tool goes back to the virtual wall surface. However it was observed that even for stiffness mismatches of $200[N/m]$ the impact on overall system performance was very negative. This does not go in accordance with the results obtained in [Cortesão et al., 2006] which show that stability problems only arise from underestimated stiffness. The results in [Cortesão et al., 2006], however, are only for a force control architecture without motion compensation capabilities (i.e. a single AOB of order 1 is tested). Further studies must be conducted to determine the double AOB architecture robustness to stiffness mismatches. A possible solution for this problem would be to implement on-line stiffness estimation.

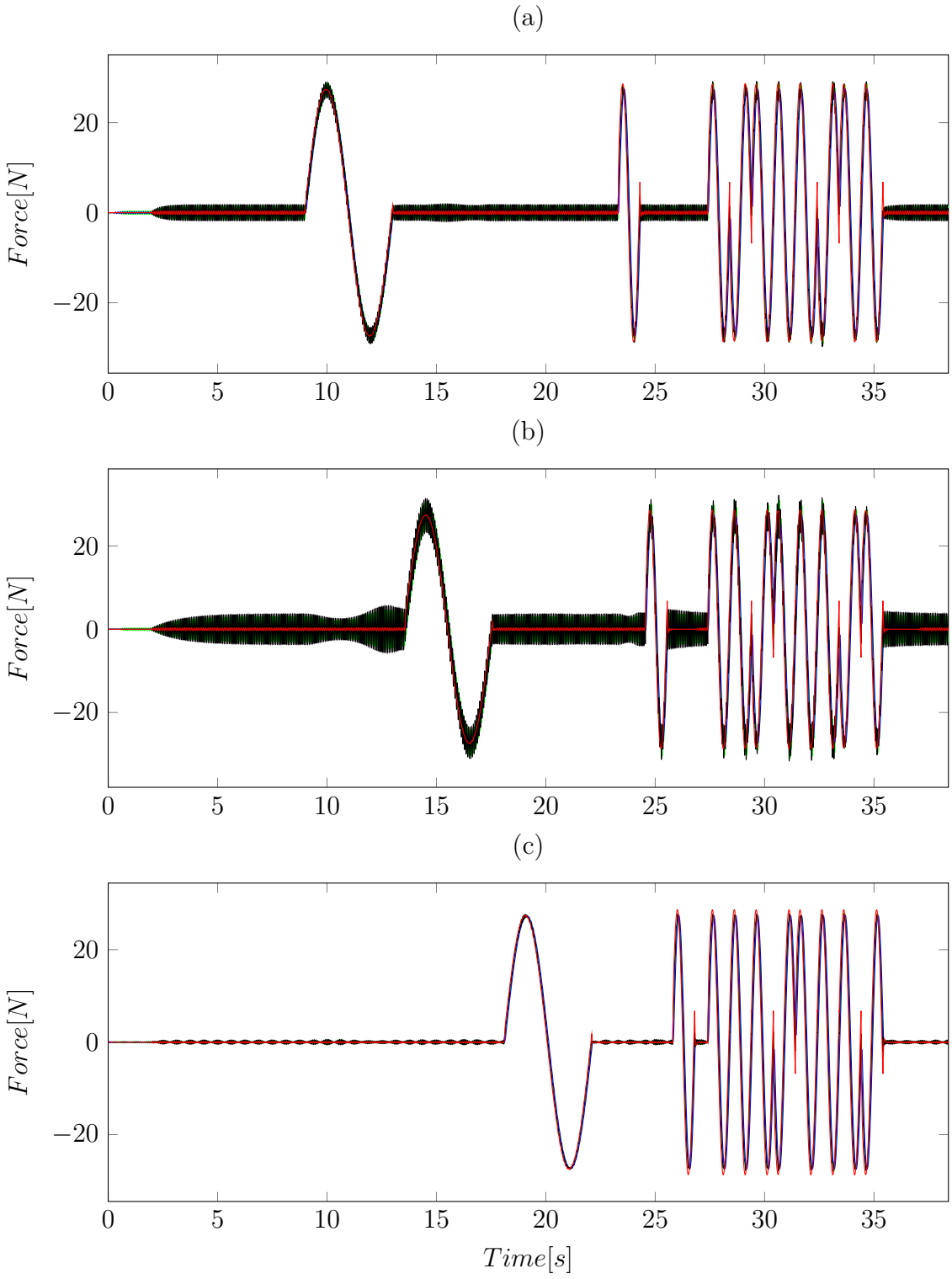

Figure 3.3: Telemanipulation coupled with double AOB force control without physiological motion. Comparison between performance with time constant $T_c = 10[ms]$ and time constant $T_c = 35[ms]$. Experimental results. Desired force F_d is represented in black and red for $T_c = 10[ms]$ and $T_c = 35[ms]$ respectively. Measured force, in green for $T_c = 10[ms]$ and blue for $T_c = 35[ms]$, for both X, Y and Z is represented in (a),(b) and (c), respectively.

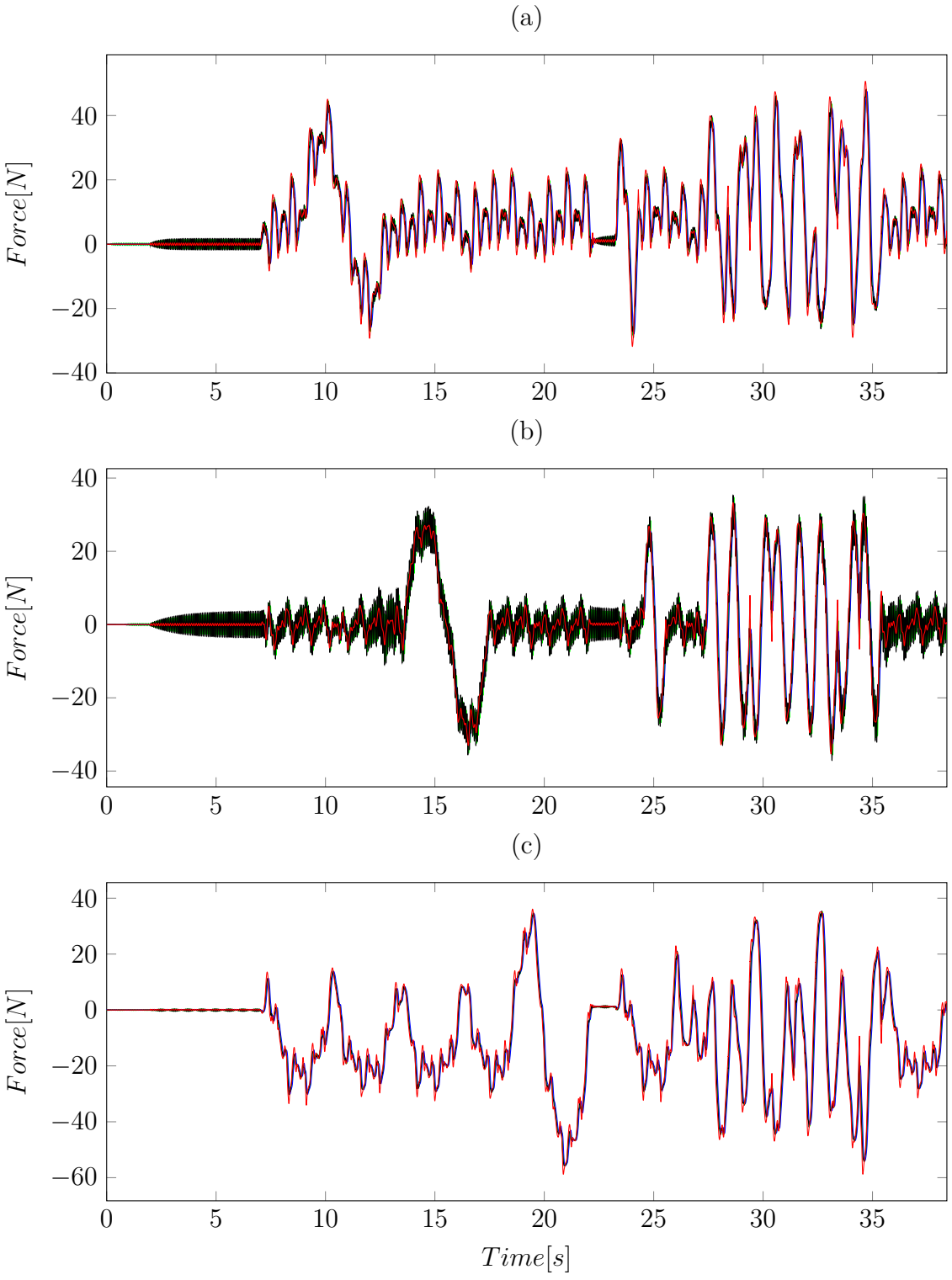

Figure 3.4: Telemanipulation coupled with double AOB force control with physiological motion. Comparison between performance with time constant $T_c = 10[ms]$ and time constant $T_c = 35[ms]$. Experimental results. Desired force F_d is represented in black and red for $T_c = 10[ms]$ and $T_c = 35[ms]$ respectively. Measured force, in green for $T_c = 10[ms]$ and blue for $T_c = 35[ms]$, for both X, Y and Z is represented in (a),(b) and (c), respectively.

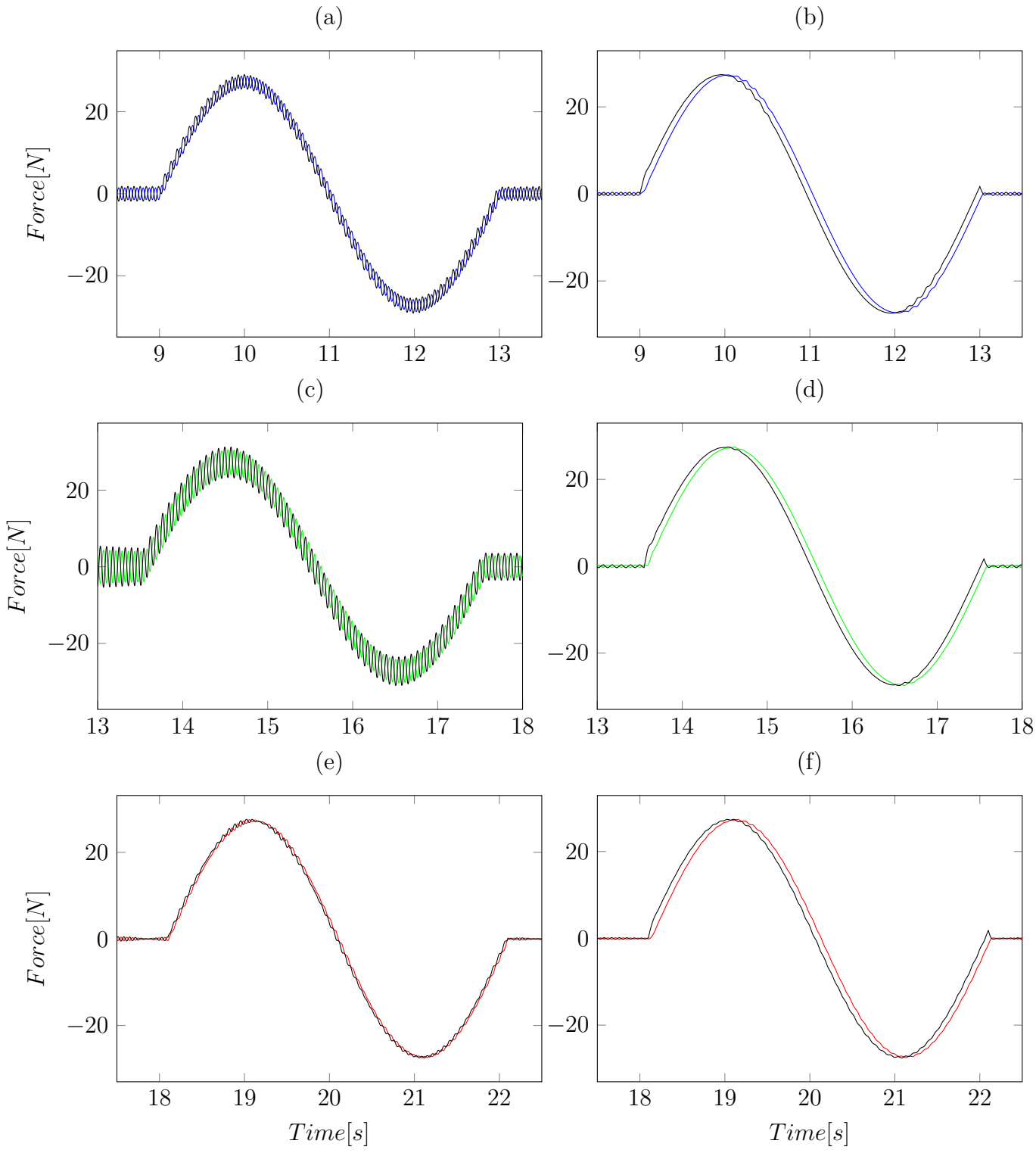

Figure 3.5: Telemanipulation coupled with double AOB force control without physiological motion. Experimental results. Desired force F_d is represented in black. Measured force for both X is represented in the first pair of images, Y in the second pair of images and Z in the third pair of images. In the left column are the results for $T_c = 10[ms]$ and in the right column the results for $T_c = 35[ms]$.

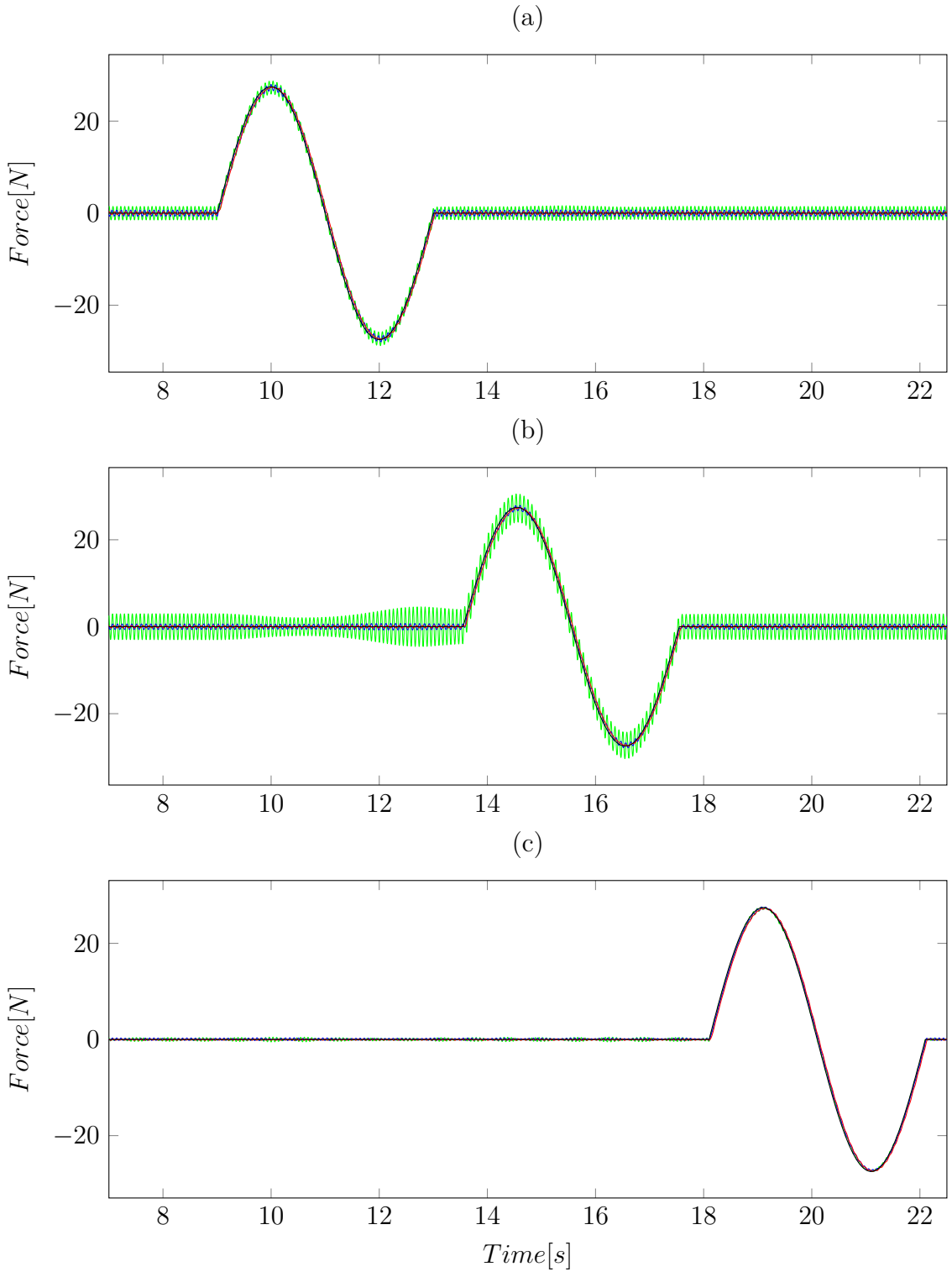

Figure 3.6: Telemanipulation coupled with double AOB force control without physiological motion. Comparison between performance for multiple time constants. Partial experimental results. Green plots for $T_c = 10[ms]$, blue plots for $T_c = 25[ms]$ and red plots for $T_c = 35[ms]$. Reference position in black has been scaled to simulate ideal desired force F_d. Measured force for both X, Y and Z is represented in (a),(b) and (c), respectively.

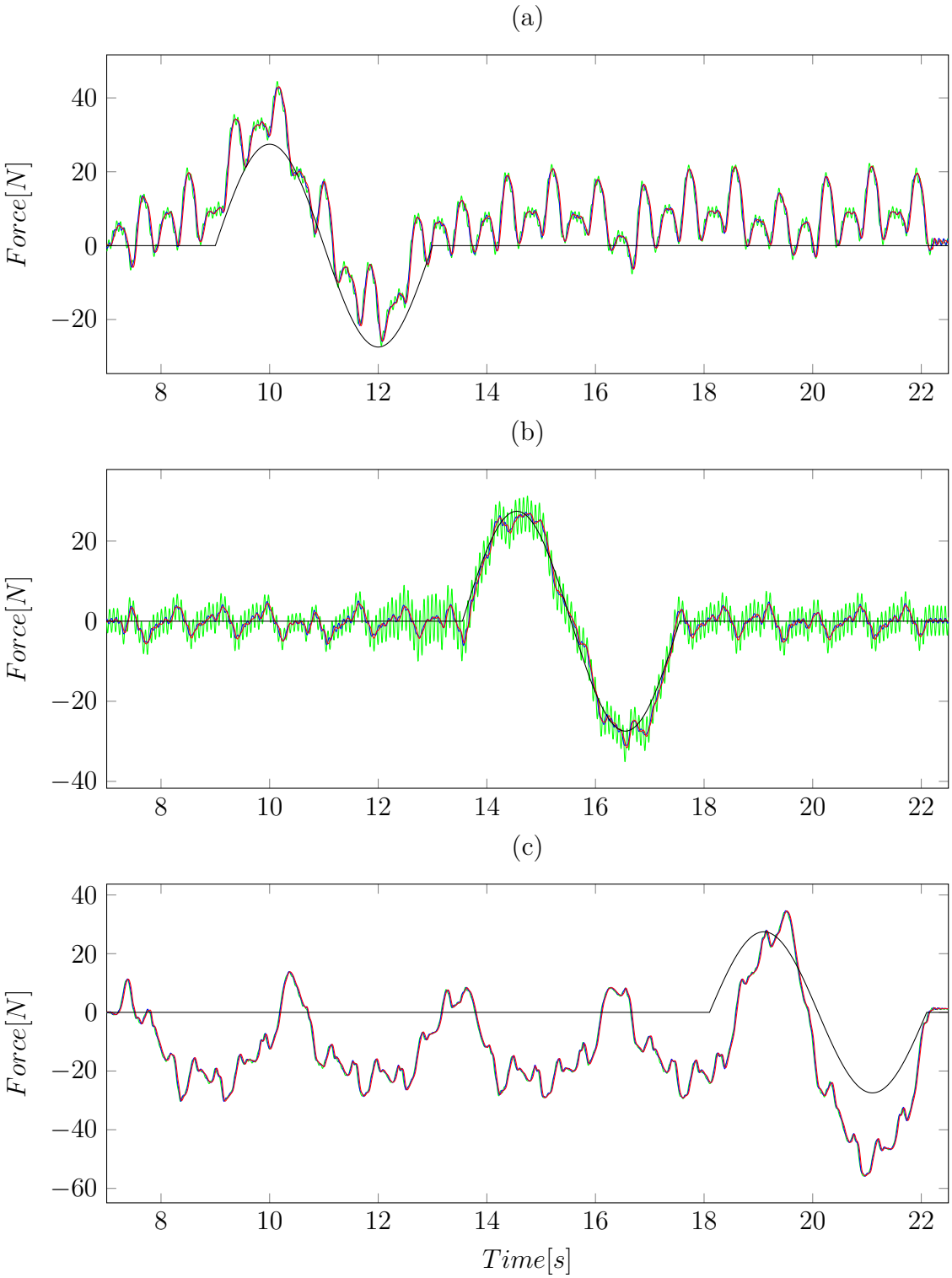

Figure 3.7: Telemanipulation coupled with double AOB force control with physiological motion. Comparison between performance for multiple time constants. Partial experimental results. Green plots for $T_c = 10[ms]$, blue plots for $T_c = 25[ms]$ and red plots for $T_c = 35[ms]$. Reference position in black has been scaled to simulate ideal desired force F_d. Measured force for both X, Y and Z is represented in (a),(b) and (c), respectively.

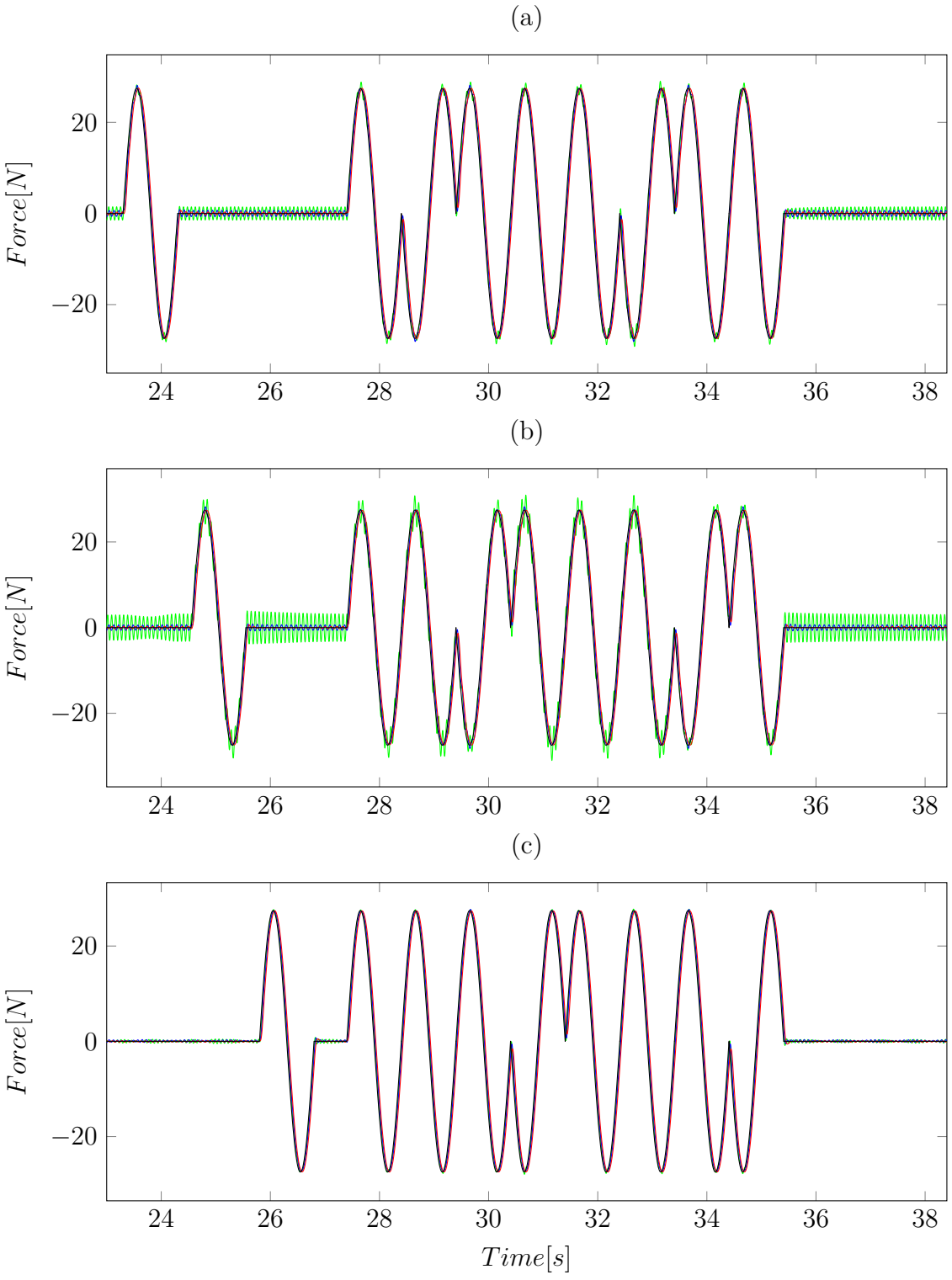

Figure 3.8: Telemanipulation coupled with double AOB force control without physiological motion. Comparison between performance for multiple time constants. Partial experimental results. Green plots for $T_c = 10[ms]$, blue plots for $T_c = 25[ms]$ and red plots for $T_c = 35[ms]$. Reference position in black has been scaled to simulate ideal desired force F_d. Measured force for both X, Y and Z is represented in (a),(b) and (c), respectively.

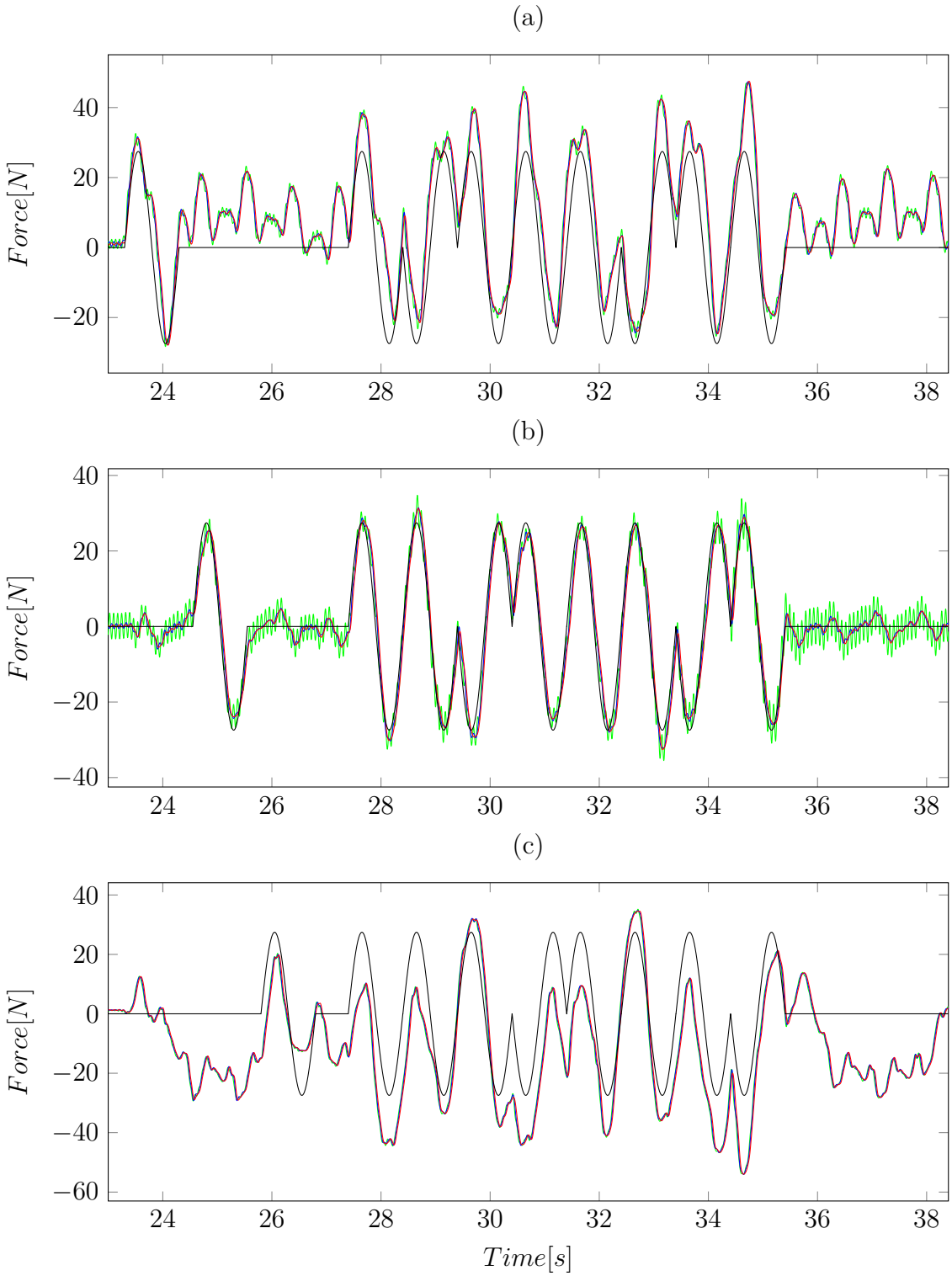

Figure 3.9: Telemanipulation coupled with double AOB force control with physiological motion. Comparison between performance for multiple time constants. Partial experimental results. Green plots for $T_c = 10[ms]$, blue plots for $T_c = 25[ms]$ and red plots for $T_c = 35[ms]$. Reference position in black has been scaled to simulate ideal desired force F_d. Measured force for both X, Y and Z is represented in (a),(b) and (c), respectively.

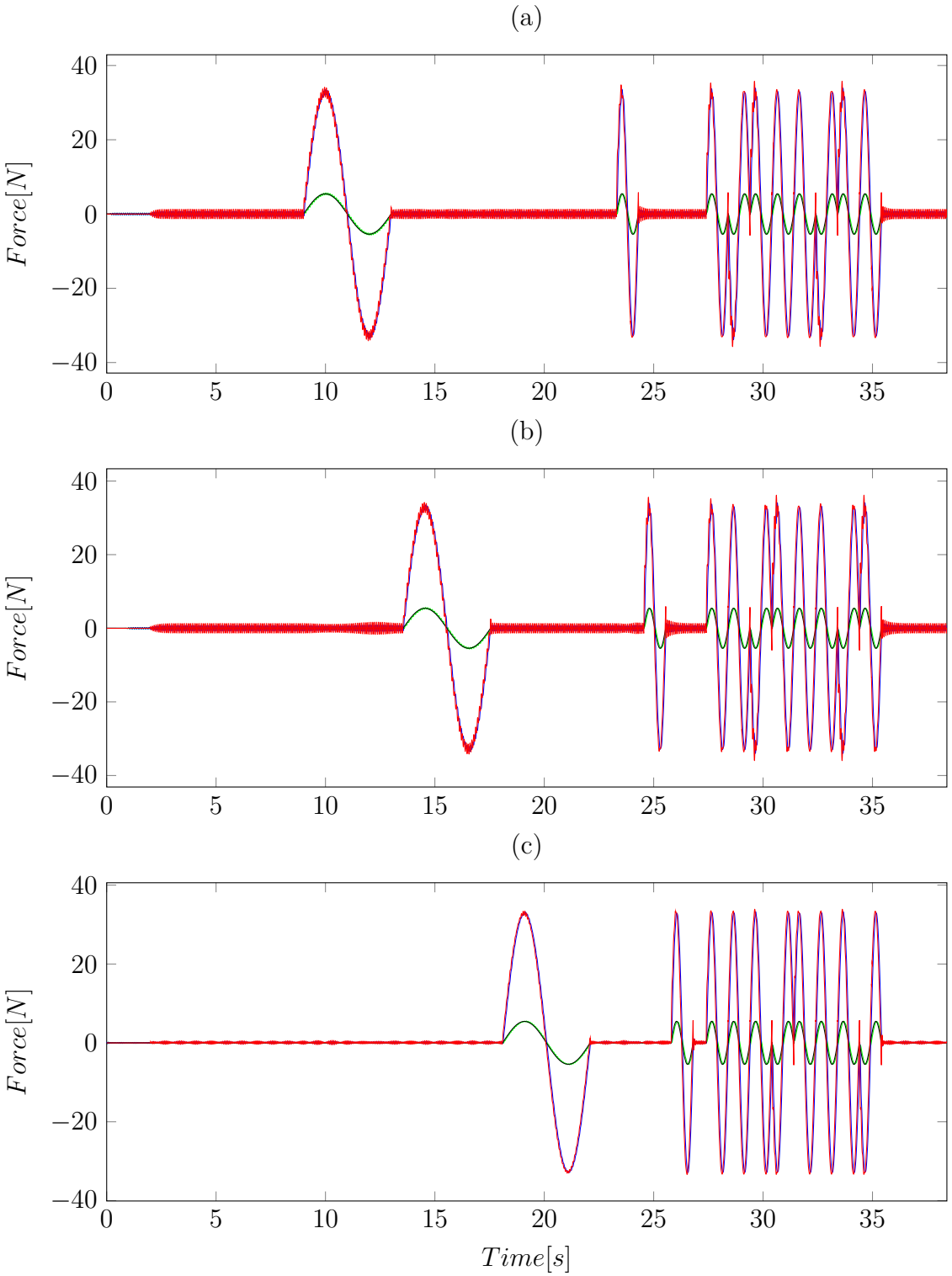

Figure 3.10: Telemanipulation coupled with double AOB force control without physiological motion. Comparison between performance with virtual coupling $K_v = 100[N/m]$ and virtual coupling $K_v = 1600[N/m]$. Experimental results. Desired force F_d is represented in black and red for $K_v = 100[N/m]$ and $K_v = 1600[N/m]$ respectively. Measured force, in green for $K_v = 100[N/m]$ and blue for $K_v = 1600[N/m]$, for both X, Y and Z is represented in (a),(b) and (c), respectively.

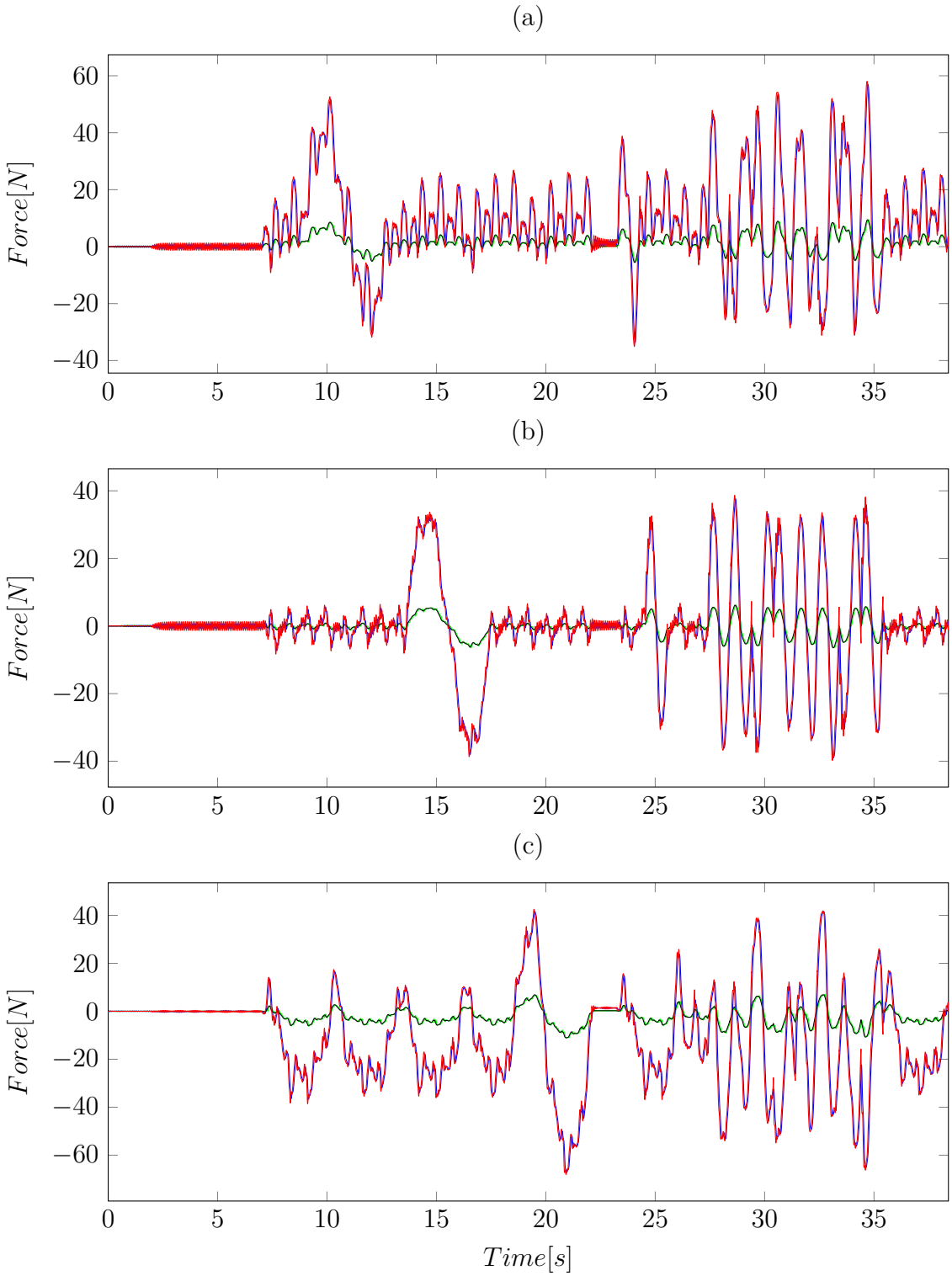

Figure 3.11: Telemanipulation coupled with double AOB force control with physiological motion. Comparison between performance with virtual coupling $K_v = 100[N/m]$ and virtual coupling $K_v = 1600[N/m]$. Experimental results. Desired force F_d is represented in black and red for $K_v = 100[N/m]$ and $K_v = 1600[N/m]$ respectively. Measured force, in green for $K_v = 100[N/m]$ and blue for $K_v = 1600[N/m]$, for both X, Y and Z is represented in (a),(b) and (c), respectively.

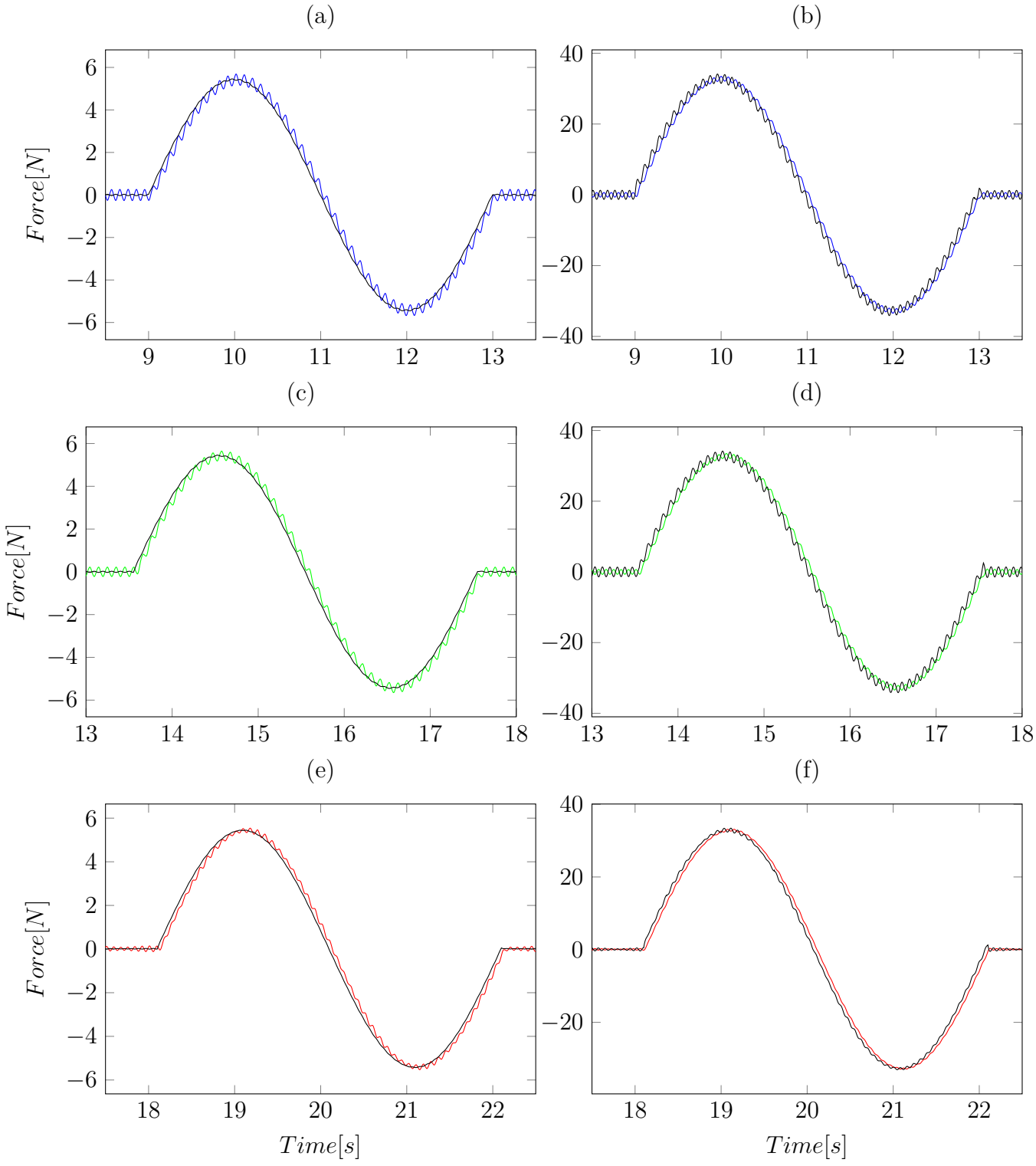

Figure 3.12: Telemanipulation coupled with double AOB force control without physiological motion. Experimental results. Desired force F_d is represented in black. Measured force for both X is represented in the first pair of images, Y in the second pair of images and Z in the third pair of images. In the left column are the results for $K_v = 100[N/m]$ and in the right column the results for $K_v = 1600[N/m]$.

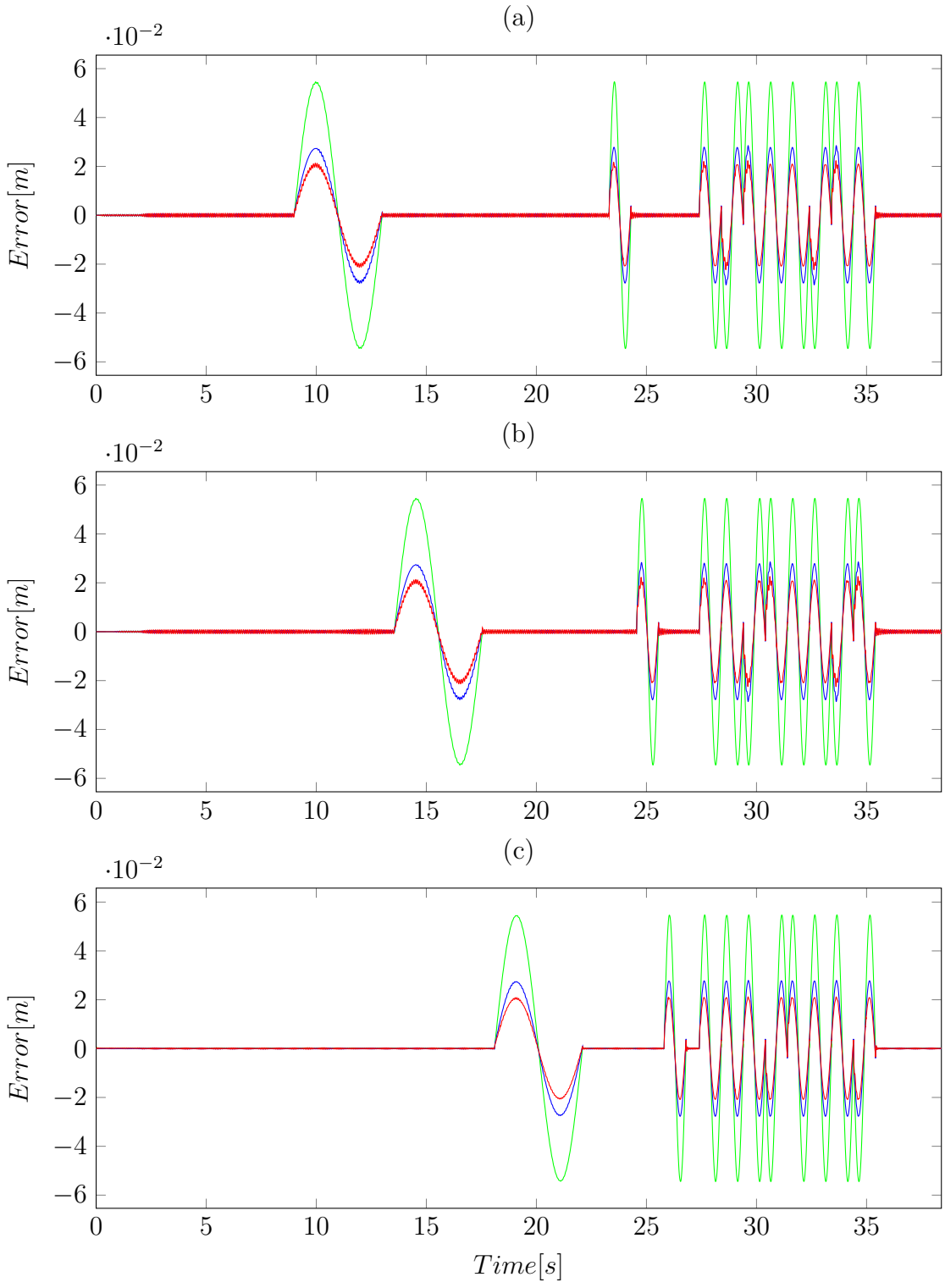

Figure 3.13: Telemanipulation coupled with double AOB force control without physiological motion. Comparison between position error of the robot end-effector regarding the master station scaled positioned. Green plots for $K_v = 100[N/m]$, blue plots for $K_v = 1000[N/m]$ and red plots for $K_v = 1600[N/m]$. Error for both X, Y and Z is represented in (a),(b) and (c), respectively.

3.2 Telemanipulation in Free-Space and Contact

3.2.1 Telemanipulation in Free-Space

Stability

The first step to achieve telemanipulation in free-space is to stabilize the system. With no changes to the control architecture (maintaining the double AOB architecture) we will always obtain a force output equal to zero ($y_k = 0$), as shown in Figure 3.14. Rewriting 2.33 as

$$\hat{x}_{e,k} = \Phi_{e,c}\hat{x}_{e,k-1} + \Gamma_e r_{k-1} + K_k \left\{ y_k - C_a \left(\Phi_{e,c}\hat{x}_{e,k-1} + \Gamma_e r_{k-1} \right) \right\} \tag{3.5}$$

in free-space it becomes

$$\hat{x}_{e,k} = \Phi^f_{e,c}\hat{x}_{e,k-1} + \Gamma^f_e r_{k-1} \tag{3.6}$$

with

$$\Phi^f_{e,c} = \left(I - K_k C_a \right) \Phi_{e,c} \tag{3.7}$$

$$\Gamma^f_e = \left(I - K_k C_a \right) \Gamma_e. \tag{3.8}$$

This leads to a free-space plant that is not stable however, stability of the system can be achieved through the teleoperation scheme as shown in 3.2 [Cortesão et al., 2006].

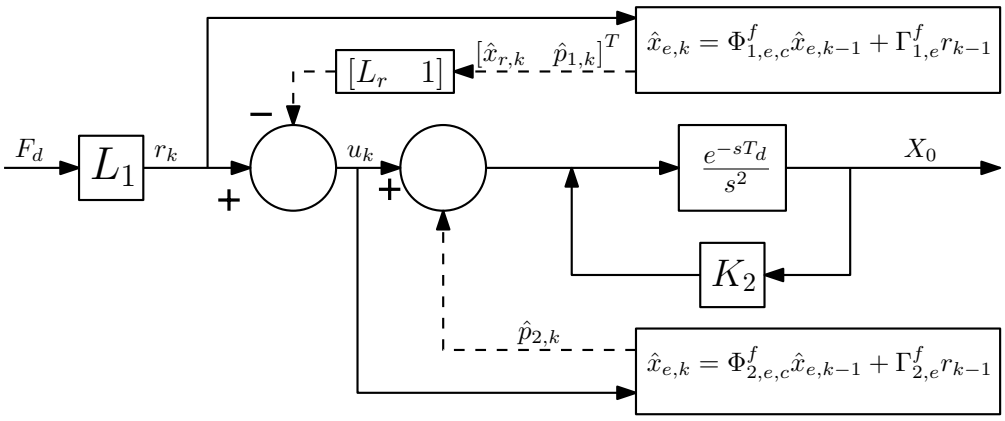

Figure 3.14: Free-space plant.

Free-space to Stiff Contact

When the robot end-effector transits from contact to free-space, and vice versa, it is necessary to adapt the double AOB stiffness. In this section we analyse the required controller

modifications to allow for online stiffness adaptation. As shown in [Cortesão et al., 2001], stiffness adaptation is possible without changing the control structure. For $K_{s,n}$ entailing the feedback gain

$$L_r = \begin{bmatrix} l_1 & l_2 & l_3 & \cdots & l_n \end{bmatrix} \tag{3.9}$$

for a change in $K_{s,n}$ of ΔK_s, the new L_r vector is given by

$$L_r = \begin{bmatrix} l_1/(1+\Delta K_s/K_{s,n}) & l_2/(1+\Delta K_s/K_{s,n}) & l_3 & \cdots & l_n \end{bmatrix}. \tag{3.10}$$

As seen, the values of L_r corresponding to the states originated by the system time delay do not need to be updated.

The state estimate must also be updated to accommodate for stiffness changes. For ΔK_s, the Φ_r matrix changes to $\Phi_r + \Delta\Phi_r$, with

$$\Delta\Phi_r = \begin{bmatrix} 0 & \Delta\Gamma_1 & 0 & \cdots & 0 \\ 0 & 0 & 0 & \cdots & 0 \\ \vdots & \vdots & \vdots & \ddots & \vdots \\ 0 & 0 & 0 & \cdots & 0 \\ 0 & 0 & 0 & \cdots & 0 \end{bmatrix}, \tag{3.11}$$

being

$$\Delta\Gamma_1 = \frac{\Delta K_s}{K_{s,n}}\Gamma_1. \tag{3.12}$$

The Kalman gains are obtained online, so they will eventually converge to their steady-state values.

For a smoother transition between free-space and stiff contact, when in proximity to the stiff surface the controller starts adjusting with lower values of ΔK_s. This is done by determining the distance between the end-effector and the stiff surface and, when it reaches a certain threshold, stiffness adaptation is made proportionally to the distance left to contact. For real life tests a camera, or distance sensor, could be used to determine the distance to the stiff surface.

3.2.2 Results and Discussion

To study the double AOB architecture capabilities of free-space movement and free-space to contact transition a simple movement along the Z axis is performed, consisting of compression and decompression of the heart surface with multiple free-space to contact transitions.

Tests are conducted without the presence of physiological motion, and in the presence of physiological motions. Physiological motions begin at 7[s], last for 15.2[s], are interrupted for 1[s], and then repeat for another 15.2[s]. In Table 3.3, the RMSE values referent to force, position in free-space and force in contact only, are presented. In Figures 3.15 and 3.17 the system behaviour is observable in force and position, respectively, without the presence of physiological motion. Figures 3.16 and 3.19 represent the error in position and force, respectively.

In general, the results obtained were sub-optimal. Even though the double AOB architecture ability for free-space movement and free-space to contact transition has been proven, the overall system performance was not as promising as former results for this control architecture. This result was mainly due to the difference in time constant between operation without telemanipulation, shown in Chapter 2, and operation with telemanipulation. Without telemanipulation the system was stable with $T_c = 3[ms]$, however with telemanipulation the best system performance corresponds to $T_c = 20[ms]$, this will, of course, impact greatly the system force tracking performance.

There were also two persistent issues that were encountered during testing. The first issue results from the transitions between contact and free-space, exclusively, even though a solution to attempt to smooth this transition was implemented, as described in the previous section. During transition, the end-effector would always experience oscillation. This may be due to the second problem encountered, which was the inability to perform tests with on-line update of the Kalman gains leading to system instability during fast transitions between contact and free-space. Even when the steady-state values of the Kalman gains for contact and free-space were used in the respective situations, the problem still persisted. As such, the steady-state values of the Kalman gains for contact were used throughout the entire operation without on-line update.

Even so, the results obtained without the presence of physiological motion are promising, with force RMSE values under 0.81 [N] which corresponds to sub-milimetric displacements, and also sub-millimetric position errors in free-space for all the three axes. The increase of K_v in free-space operation entailed higher precision, however, the instability issue during transitions worsened, so a value of $K_v = 1600[N/m]$ was chosen for free-space operation.

Table 3.3: RMSE of the force and position for telemanipulation with free-space to contact transitions. Values for force error during contact in the presence of physiological motion ($FRMSE_{HeartOn}$), values for force error during contact without physiological motion ($FRMSE_{HeartOff}$), and values for position error in free-space, in millimetres, during operation without physiological motion ($PRMSE_{Free}$).

	$FRMSE_{HeartOn}$	$FRMSE_{HeartOff}$	$PRMSE_{Free}$
X axis $[N]$	6.2550	0.6816	0.2524
Y axis $[N]$	2.6930	0.7798	0.3267
Z axis $[N]$	2.7445	0.2584	0.1161

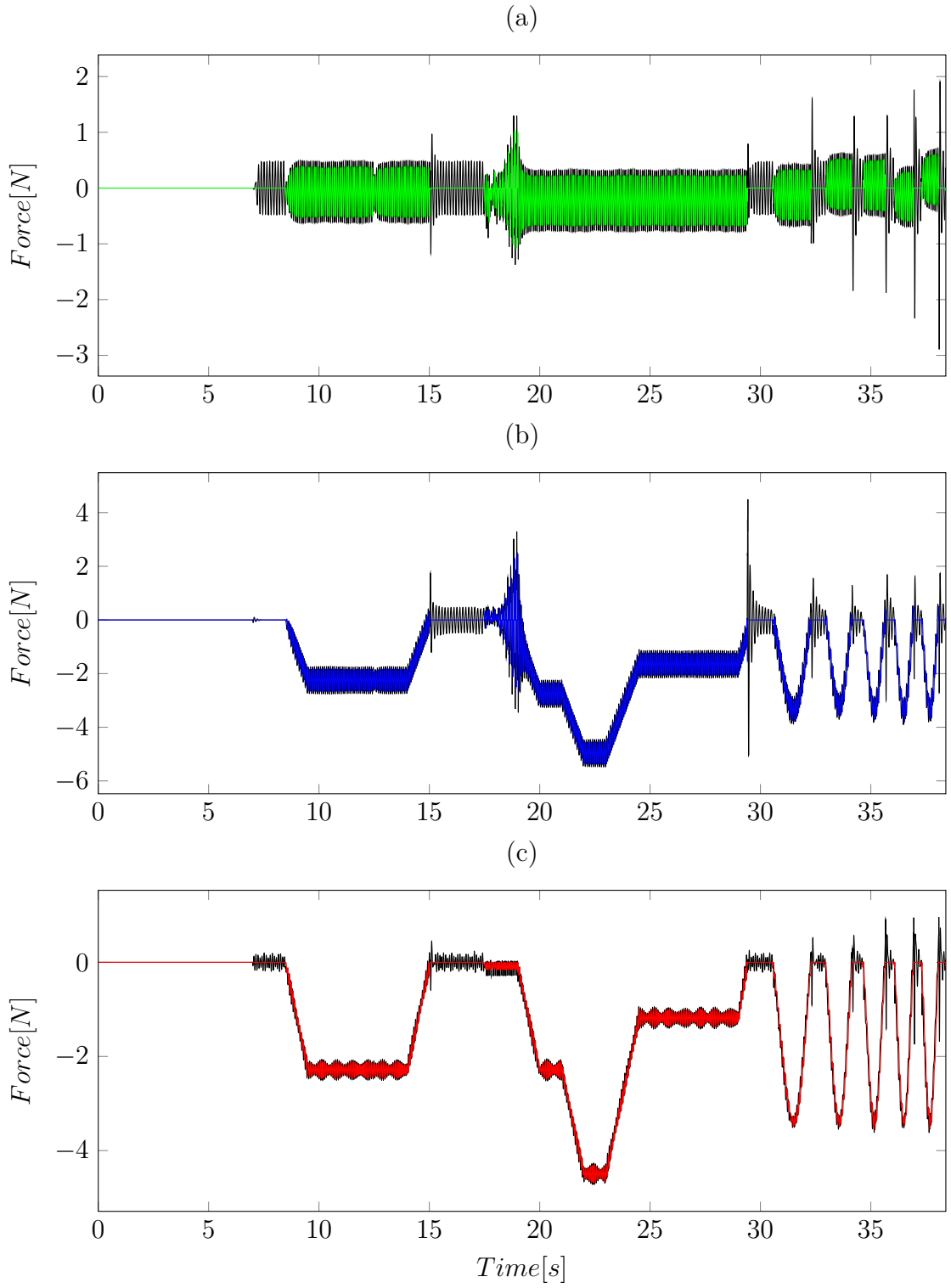

Figure 3.15: Telemanipulation with free-space to contact transitions without physiological motion. Force results for X, Y and Z are represented in (a),(b) and (c), respectively. Reference force F_d represented in black.

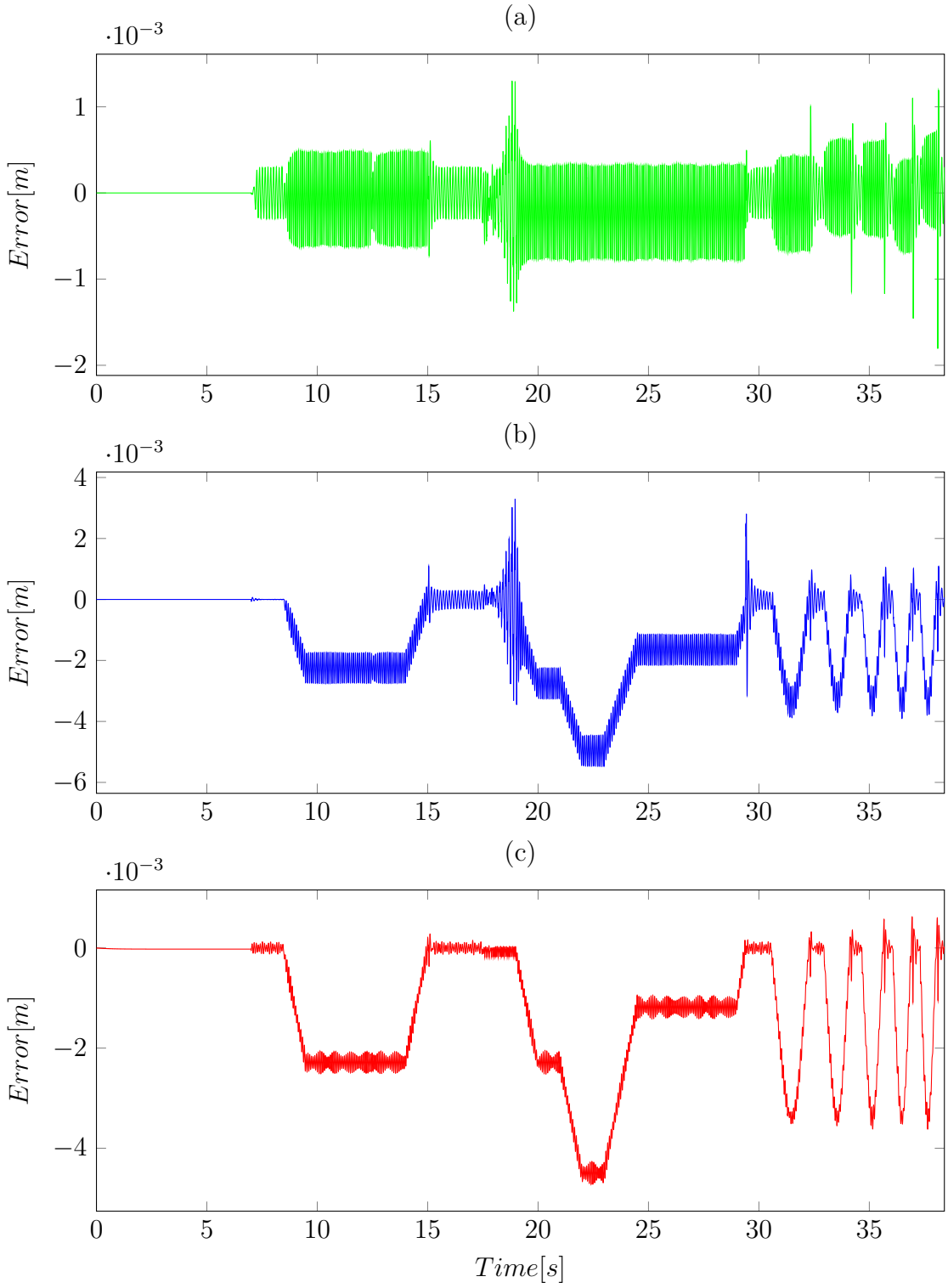

Figure 3.16: Telemanipulation with free-space to contact transitions without physiological motion. Position error results for X, Y and Z are represented in (a),(b) and (c), respectively.

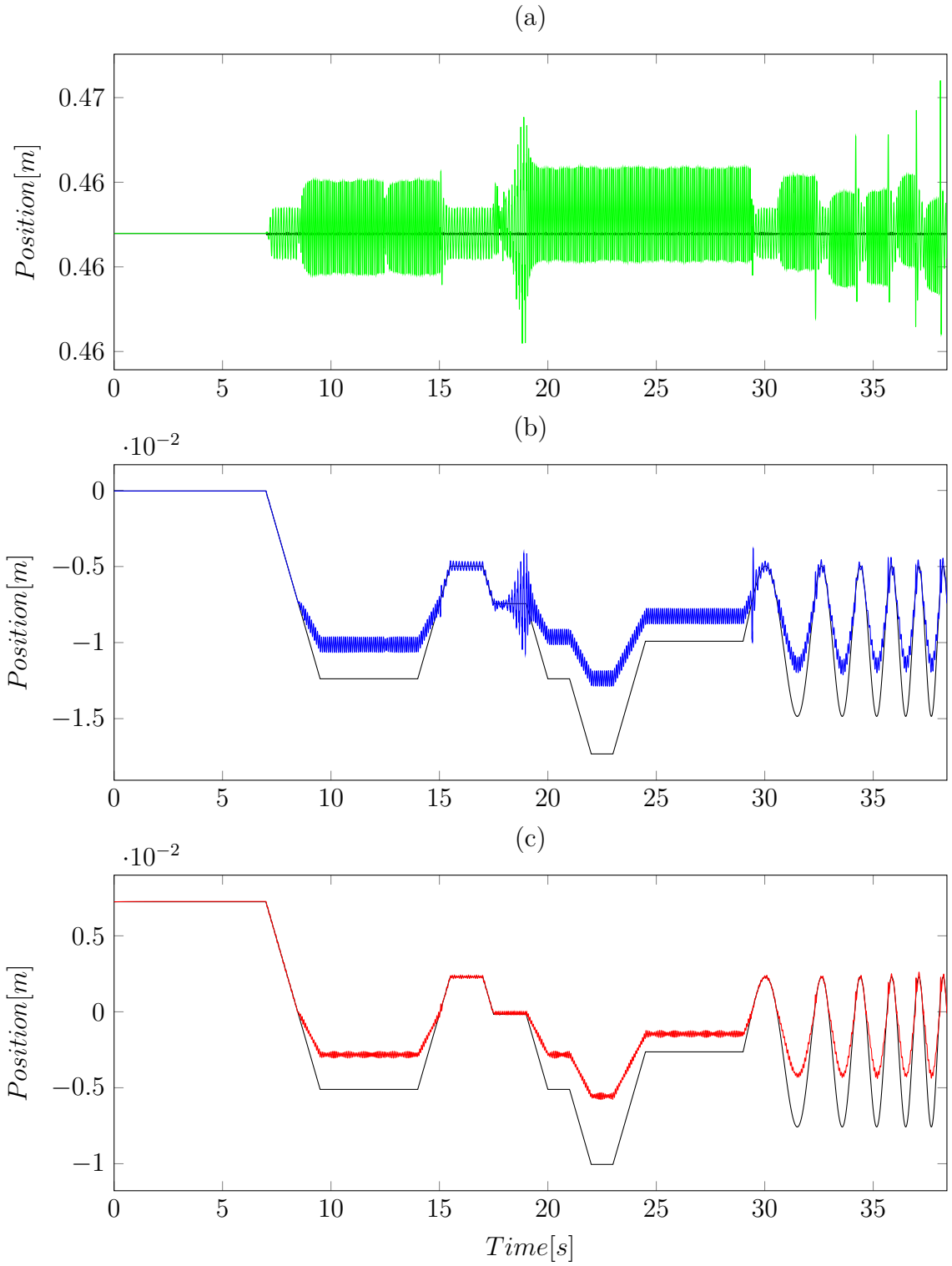

Figure 3.17: Telemanipulation with free-space to contact transitions without physiological motion. Comparison between position reference (black plots) and the position of the robot end-effector (coloured plots). Plots for X, Y and Z are represented in (a),(b) and (c), respectively.

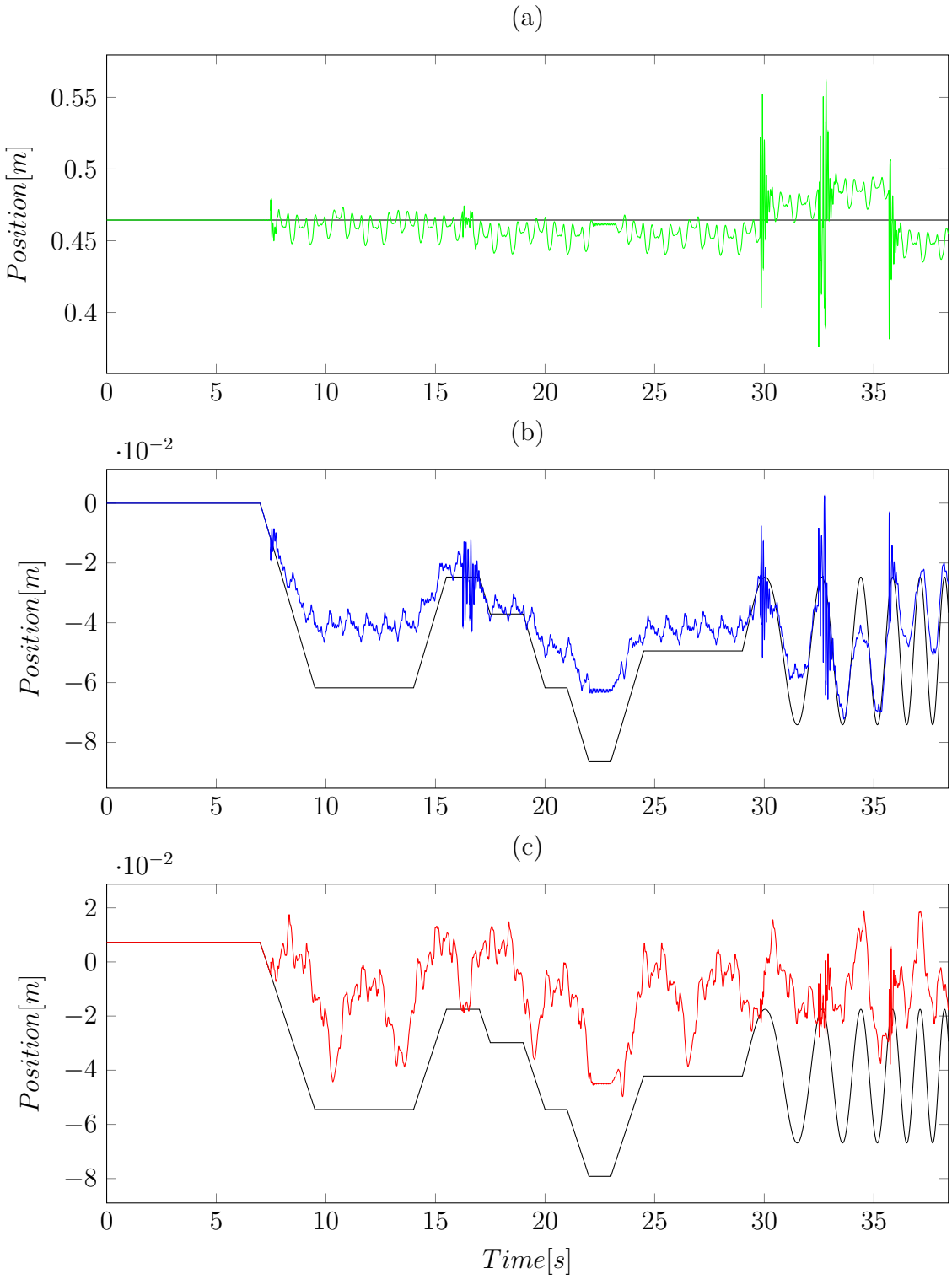

Figure 3.18: Telemanipulation with free-space to contact transitions with physiological motion. Comparison between position reference (black plots) and the position of the robot end-effector (coloured plots). Plots for X, Y and Z are represented in (a),(b) and (c), respectively.

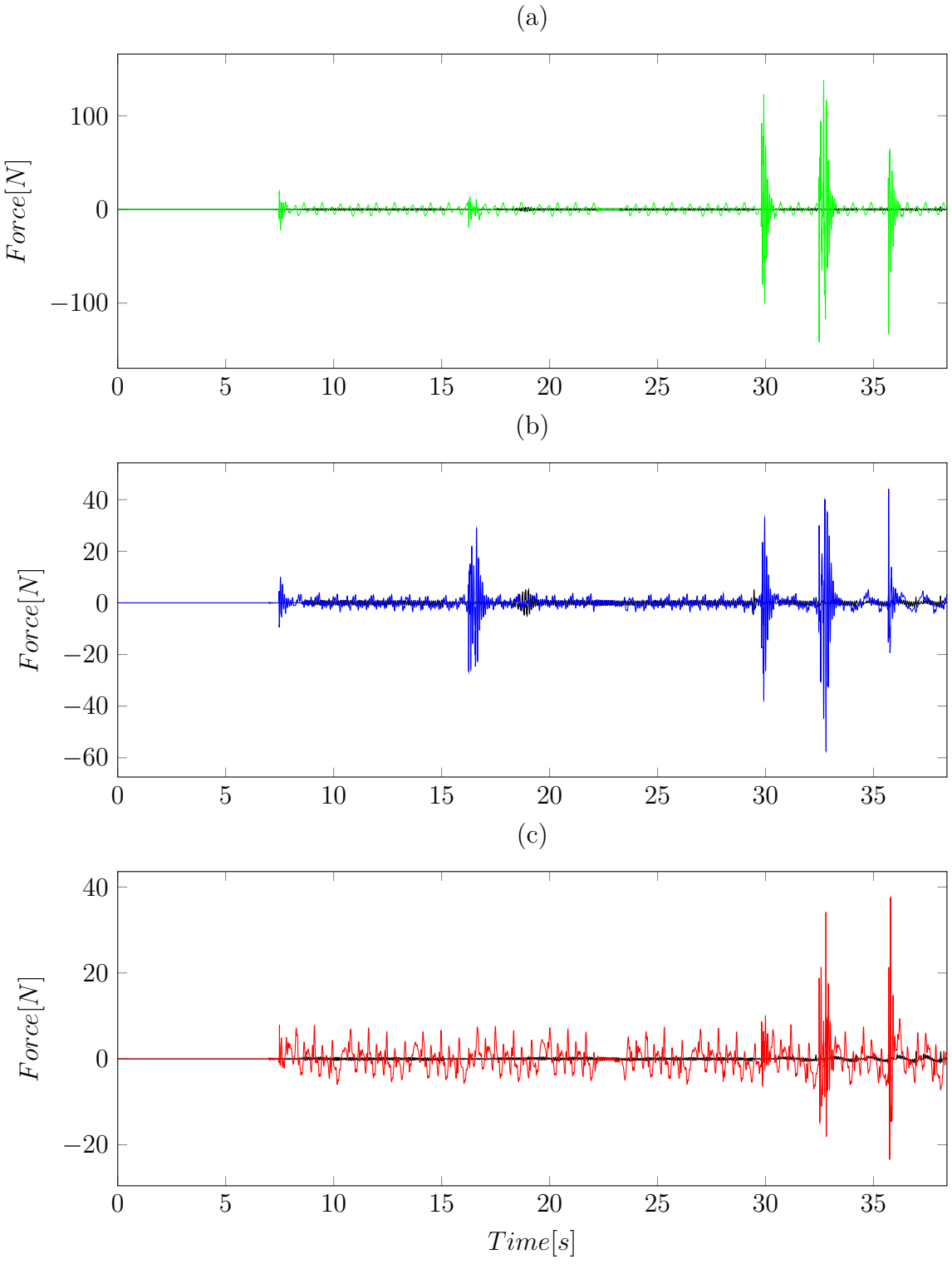

Figure 3.19: Telemanipulation with free-space to contact transitions. Comparison between force error in the presence of physiological motion and force error without physiological motion. Plots for X, Y and Z are represented in (a),(b) and (c), respectively. Coloured plots represent results with physiological motion and black plots represent results without physiological motion.

4 Conclusion

In this thesis a solution for physiological motion compensation during heart surgery is proposed. Based on modified Kalman filters, a double AOB force control architecture is proposed. This architecture consists of two AOBs, one responsible for compensating system disturbances and set the system dynamics for force control, and the second AOB is merely responsible for physiological motion compensation. The control capabilities of the double AOB architecture have been studied in previous literature, and its viability proved in *in-vivo* experiments. As such, the first step is to provide and validate a simulated robot and environment to allow for further testing of the double AOB architecture in *ex-vivo* experiments. For this, the proposed control architecture is implemented in the simulator and the system performance is compared to the one previously obtained in the literature. Afterwards, telemanipulation capabilities with haptic feedback are implemented and tested for the double AOB architecture. First and foremost, tests in contact with the environment are conducted and the control parameters are tuned. Sub-sequentially, free-space to contact transitions and free-space behaviour are implemented and tested.

The results obtained show that the system behaved as expected on the simulator, with even better performance due to the absence of system model mismatches and other unforeseen disturbances. Concerning telemanipulation, tests were conducted with constant contact to fine tune the control parameters. Results showed that the double AOB architecture performed well under telemanipulation with good position tracking and with capability for telepresence, however, not without repercussions in force tracking with a significant increase of RMSE values around 3 $[N]$. Finally, for free-space telemanipulation several issues were encountered and the overall system performance was not as favourable as hoped. The double AOB controller is indeed capable of free-space operation but the performance could not be optimised. Even so, there were some promising results and there is room for improvement, such as improving the smooth transitions and attempt to remedy the effect of on-line Kalman

gain estimation during transitions.

Further development of the double AOB control architecture may include the implementation of online stiffness estimation and orientation control, especially since the WAM robot is prepared for 7 DoF and the simulator used allows for testing in this configuration.

5 Bibliography

[American Heart Association, 2017] American Heart Association (2017). Cardiac Procedures and Surgeries, Bypass Surgery.

[Ascione et al., 2000] Ascione, R., Lloyd, C. T., Underwood, M. J., Lotto, A. A., Pitsis, A. A., and Angelini, G. D. (2000). Inflammatory response after coronary revascularization with or without cardiopulmonary bypass. *The Annals of thoracic surgery*, 69(4):1198–204.

[Åström and Wittenmark, 1997] Åström, K. J. and Wittenmark, B. (1997). *Computer-Controlled Systems: Theory and Design, Third Edition*.

[Bachta et al., 2011] Bachta, W., Renaud, P., Laroche, E., Forgione, A., and Gangloff, J. (2011). Active stabilization for robotized beating heart surgery. *IEEE Transactions on Robotics*, 27(4):757–768.

[Bebek and Çavu\Cso\Uglu, 2007] Bebek, Ö. and Çavu\Cso\Uglu, M. C. (2007). Intelligent Control Algorithms for Robotic-Assisted Beating Heart Surgery. *IEEE Transactions on Robotics*, 23(3):468–480.

[Benetti FJ, Ballester C, 1994] Benetti FJ, Ballester C, B. A. (1994). Uso de la Toracoscopía en cirugía coronaria para disección de la mamaria izquierda. *La Prensa Médica Argentina*, 9:81–87.

[Cagneau et al., 2007] Cagneau, B., Zemiti, N., Bellot, D., and Morel, G. (2007). Physiological Motion Compensation in Robotized Surgery using Force Feedback Control. *Proceedings 2007 IEEE International Conference on Robotics and Automation*, (April):10–14.

[Cortesão, 2007] Cortesão, R. (2007). On Kalman active observers. *Journal of Intelligent and Robotic Systems: Theory and Applications*, 48(2):131–155.

[Cortesão and Dominici, 2017] Cortesão, R. and Dominici, M. (2017). Robot Force Control on a Beating Heart. *IEEE/ASME Transactions on Mechatronics*, PP(99):1–1.

[Cortesão et al., 2001] Cortesão, R., Koeppe, R., Nunes, U., and Hirzinger, G. (2001). Compliant motion control with stochastic active observers. *IEEE International Conference on Intelligent Robots and Systems*, 4:1876–1881.

[Cortesão et al., 2006] Cortesão, R., Park, J., and Khatib, O. (2006). Real-time adaptive control for haptic telemanipulation with Kalman active observers. *IEEE Transactions on Robotics*, 22(5):987–999.

[Cortesão, 2002] Cortesão, R. P. D. (2002). *Kalman Techniques for Intelligent Control Systems: Theory and Robotic Experiments*. PhD thesis, University of Coimbra.

[Gagne et al., 2012] Gagne, J., Piccin, O., Laroche, É., Diana, M., and Gangloff, J. (2012). GyroLock: Stabilizing the heart with control moment gyroscope (CMG)-From concept to first in vivo assessments. *IEEE Transactions on Robotics*, 28(4):942–954.

[Ginhoux et al., 2005] Ginhoux, R., Gangloff, J., de Mathelin, M., Soler, L., Arenas Sanchez, M. M., and Marescaux, J. (2005). Active filtering of physiological motion in robotized surgery using predictive control. *IEEE Transactions on Robotics*, 21(1):67–79.

[Hart et al., 2002] Hart, J. C., Puskas, J. D., and Sabik, J. F. (2002). Off-pump coronary revascularization: Current state of the art. *Seminars in Thoracic and Cardiovascular Surgery*, 14(1):70–81.

[Hemmerling et al., 2013] Hemmerling, T. M., Romano, G., Terrasini, N., and Noiseux, N. (2013). Anesthesia for off-pump coronary artery bypass surgery. *Annals of cardiac anaesthesia*, 16(1):28–39.

[Investigators, 2002] Investigators, T. S. (2002). Coronary artery bypass surgery versus percutaneous coronary intervention with stent implantation in patients with multivessel coronary artery disease (the Stent or Surgery trial): a randomised controlled trial. *Lancet*, 360(9338):965–70.

[Kesner and Howe, 2014] Kesner, S. B. and Howe, R. D. (2014). Robotic catheter cardiac ablation combining ultrasound guidance and force control. *International Journal of Robotics Research*, 33(4):631–644.

[Khatib, 1987] Khatib, O. (1987). A unified approach for motion and force control of robot manipulators: The operational space formulation. *IEEE Journal on Robotics and Automation*, 3(1):43–53.

[Khoshnam and Patel, 2014] Khoshnam, M. and Patel, R. V. (2014). Robotics-assisted catheter manipulation for improving cardiac ablation efficiency. *Biomedical Robotics and Biomechatronics (2014 5th IEEE RAS & EMBS International Conference on*, pages 308–313.

[Klesius et al., 2004] Klesius, A. A., Dzemali, O., Simon, A., Kleine, P., Abdel-Rahman, U., Herzog, C., Wimmer-Greinecker, G., and Moritz, A. (2004). Successful treatment of deep sternal infections following open heart surgery by bilateral pectoralis major flaps. *European Journal of Cardio-thoracic Surgery*, 25(2):218–223.

[Kolessov, 1967] Kolessov, V. I. (1967). Mammary artery-coronary artery anastomosis as method of treatment for angina pectoris. *The Journal of thoracic and cardiovascular surgery*, 54(4):535–544.

[Larsson, 2015] Larsson, H. (2015). *Blausen gallery 2014*. PhD thesis.

[Lemma et al., 2005] Lemma, M., Mangini, A., Redaelli, A., and Acocella, F. (2005). Do cardiac stabilizers really stabilize? Experimental quantitative analysis of mechanical stabilization. *Interactive cardiovascular and thoracic surgery*, 4(3):222–6.

[Lönn et al., 1999] Lönn, U., Peterzén, B., Carnstam, B., and Casimir-Ahn, H. (1999). Beating heart coronary surgery supported by an axial blood flow pump. *Annals of Thoracic Surgery*, 67(1):99–104.

[MedMarket Diligence, 2016] MedMarket Diligence (2016). The Evolution of Coronary Revascularization Markets.

[Nakamura et al., 2001] Nakamura, Y., Kishi, K., and Kawakami, H. (2001). Heartbeat synchronization for robotic cardiac surgery. In *Proceedings - IEEE International Conference on Robotics and Automation*, volume 2, pages 2014–2019.

[Patronik et al., 2011] Patronik, N. A., Ota, T., Zenati, M. A., and Riviere, C. N. (2011). Synchronization of epicardial crawling robot with heartbeat and respiration for improved

safety and efficiency of locomotion. *The international journal of medical robotics + computer assisted surgery : MRCAS*, 7(April):375–392.

[Ruszkowski et al., 2015] Ruszkowski, A., Mohareri, O., Lichtenstein, S., Cook, R., and Salcudean, S. (2015). On the feasibility of heart motion compensation on the daVinci® surgical robot for coronary artery bypass surgery: Implementation and user studies. In *Proceedings - IEEE International Conference on Robotics and Automation*, volume 2015-June, pages 4432–4439.

[Sauvée et al., 2007] Sauvée, M., Noce, A., Poignet, P., Triboulet, J., and Dombre, E. (2007). Three-dimensional heart motion estimation using endoscopic monocular vision system: From artificial landmarks to texture analysis. *Biomedical Signal Processing and Control*, 2(3):199–207.

[Serruys et al., 2009] Serruys, P. W., Morice, M.-C., Kappetein, A. P., Colombo, A., Holmes, D. R., Mack, M. J., Ståhle, E., Feldman, T. E., van den Brand, M., Bass, E. J., Van Dyck, N., Leadley, K., Dawkins, K. D., and Mohr, F. W. (2009). Percutaneous Coronary Intervention versus Coronary-Artery Bypass Grafting for Severe Coronary Artery Disease. *New England Journal of Medicine*, 360(10):961–972.

[Slogoff et al., 1982] Slogoff, S., Girgis, K. Z., and Keats, a. S. (1982). Etiologic factors in neuropsychiatric complications associated with cardiopulmonary bypass. *Anesthesia and analgesia*, 61(11):903–911.

[Trejos et al., 1999] Trejos, A. L., Salcudean, S. E., Sassani, F., and Lichtenstein, S. (1999). On the Feasibility of a Moving Support for Surgery on the Beating Heart. *Medical Image Computing and Computer-Assisted Intervention MICCAI'99*, pages 1088–1098.

[World Health Organization, 2017] World Health Organization (2017). Cardiovascular Diseases.

[Yuen et al., 2010a] Yuen, S. G., Dubec, K. A., and Howe, R. D. (2010a). Haptic noise cancellation: Restoring force perception in robotically-assisted beating heart surgery. In *2010 IEEE Haptics Symposium, HAPTICS 2010*, pages 387–392.

[Yuen et al., 2010b] Yuen, S. G., Perrin, D. P., Vasilyev, N. V., Nido, P. J., and Howe, R. D. (2010b). Force tracking with feed-forward motion estimation for beating heart surgery. *IEEE Transactions on Robotics*, 26(5):888–896.

[Zarrouk et al., 2013] Zarrouk, Z., Chemori, A., and Poignet, P. (2013). Force feedback control for compensation of physiological motions in beating heart surgery with real-time experiments. *2013 3rd International Conference on Systems and Control, ICSC 2013*, pages 956–961.